Immune Checkpoint Blockade induces peripheral cytotoxicity and persistence of large effector CD8$^+$ T cell clones

Watson RA[1,2,3,⊗], Tong O[1,2,⊗], Cooper R[1,2], Taylor CA[1,2], Verge de Los Aires A[1,2], Mahé EA[1,2], Nassiri I[1,2], Middleton MR[2,3], Fairfax BP[1,2,3,*]

1. MRC Weatherall Institute of Molecular Medicine, University of Oxford, Headington, Oxford, United Kingdom, OX3 9DU
2. Department of Oncology, University of Oxford, Old Road Campus Research Building, Oxford, United Kingdom, OX3 7DQ
3. Oxford Cancer and Haematology Centre, Oxford University Hospitals NHS Foundation Trust, Churchill Hospital, Oxford, United Kingdom, OX3 7LE

[⊗] These authors contributed equally to this work

* To whom correspondence should be addressed:

Dr Benjamin Fairfax; benjamin.fairfax@oncology.ox.ac.uk

ONE SENTENCE SUMMARY

Using single-cell and bulk transcriptomics we show that checkpoint immunotherapy has divergent effects on $CD8^+$ T cells, with the impact on cell division and gene expression determined by the baseline clone size and phenotype of the cell; these findings have ramifications for our understanding of inter-individual variation in response to treatment.

ABSTRACT

Immune checkpoint blockers (ICB) exert their anti-cancer effects via $CD8^+$ T cells, although how responses vary over sub-populations and across clones is incompletely understood. We performed single-cell RNA-sequencing of $CD8^+$ T cells and their receptors pre and post ICB across eight patients, integrating results with bulk-sequencing data (n=169). We identify seven phenotypic subsets with divergent sensitivity to ICB, finding the effector subset demonstrates the most pronounced changes. ICB response was related to clone size, with small and large clones markedly differing in the magnitude and immunological relevance of regulated genes. ICB upregulates mitotic pathways and promotes expansion and survival of larger, more cytotoxic clones. Notably, baseline cytotoxicity, but not correlates of mitosis, associated with progression-free survival; highlighting the importance of the pre-treatment $CD8^+$ immune landscape in long-term response. This work further advances understanding of the molecular determinants of ICB response and assists in the search for peripheral prognostic biomarkers.

35 **INTRODUCTION**

36 Antibodies binding the checkpoint proteins CTLA4 (cytotoxic T-lymphocyte-associated protein 4) and
37 PD-1 (programmed cell death protein 1) – Immune Checkpoint Blockers (ICBs) – have revolutionised
38 the treatment of metastatic melanoma (MM) and numerous other cancers*(1, 2)*. There is, however,
39 marked heterogeneity in ICB-induced clinical benefit*(2)* and insights into determinants of ICB activity
40 and variation in clinical response remain limited. Although tumour mutational burden has been linked
41 to clinical outcome across multiple cancers*(3, 4)*, its absolute importance is unclear*(5)*. Similarly, the
42 prognostically favourable association of tumour infiltrating lymphocytes (TILs) is long-established, but
43 factors controlling T cell infiltration remain unresolved*(6, 7)*. Crucially, it is increasingly apparent that
44 general aspects of immune function may play a critical, yet comparatively under-investigated role in
45 determining tumour recognition and control*(8)*.

46 $CD8^+$ T cells are cardinal to the immune response against MM*(9)* and much work has focussed on the
47 response seen in pre-existing TILs*(10, 11)*. However, recent studies in non-melanoma skin cancer have
48 shown that the T cell response to ICB derives from a distinct repertoire of T cell clones, denoted by
49 shared carriage of specific T cell receptors (TCR), that may have recently migrated to the tumour*(12)*.
50 Shared T cell clones can be observed within both cancers and blood of MM patients*(11, 13–15)*, whilst
51 the number of peripheral expanded clones (occupying >0.5% of the repertoire) post-ICB is associated
52 with long-term response to treatment*(16)*. Taken together, it is evident the clonal T cell response to ICB
53 detected in peripheral blood can provide relevant insights into immune-control of cancer and may allow
54 for on-treatment prognostication. Nonetheless, there are several unresolved questions regarding the
55 effect of ICB at the level of T cell clones. Centrally, the determinants of ICB response across subsets
56 and on a clone-by-clone basis are unresolved. The T cell ICB response has multiple, potentially
57 orthogonal, components, including mitotic cell division*(17)* and increased cytotoxicity as exemplified
58 by interferon gamma (IFNγ) induction*(18)*. Whether these responses vary according to T cell subset*(19)*,
59 their heterogeneity across clones and if they are derived from novel or pre-existing clones is unknown.

60 To explore the peripheral CD8$^+$ T cell response to ICB we have used single cell RNA-sequencing
61 (scRNA-seq) to track the transcriptomic response of individual T cell clones to ICB treatment,
62 identifying baseline markers of clonal sensitivity to ICB, and charting how response varies according
63 to phenotypic subset and clonal size. We indeed find that T cell responses to ICB vary substantially
64 according to clonal size and phenotypic subset. Effector T cells show notably increased responsivity to
65 ICB but remain proportionally stable with treatment – instead, ICB drives an increase in a subset of
66 highly cycling, but phenotypically exhausted mitotic cells which, by and large, fail to clonally expand.
67 Further dissection of ICB response according to clonal size reveals that basal gene expression and
68 changes imparted by treatment vary markedly, with larger T cell clones developing enhanced TCR
69 signalling compared to all other clones. Finally, by tracking TCRs over longer periods of treatment we
70 identify markers of clonal persistence following ICB, demonstrating that ICB promotes expansion and
71 survival of pre-existing large, cytotoxic T cell clones; indicating that the effectiveness of ICB is dictated
72 by the baseline immune state.

73 **RESULTS**

74 **Single-cell profiling of peripheral CD8$^+$ T cells from patients with metastatic melanoma**

75 We generated paired baseline (day 0 – 'C1') and on-treatment (day 21 – 'C2') 5' scRNA-seq and V(D)J
76 profiles across peripheral CD8$^+$ T cells from eight patients with MM undergoing treatment with cICB
77 (ipilimumab plus nivolumab, n=4) or sICB (pembrolizumab, n=4) (**fig. 1a; table S1; Methods**). In
78 total, 22,445 *CD3*/*CD8* expressing cells passed quality control, of which 17,909 cells had TCR
79 sequences, with similar distribution across C1 and C2 samples (**fig S1a**). To identify distinct CD8$^+$ T
80 cell populations, we performed unsupervised clustering and subsequently cross-referenced each cluster
81 to reference identities from published CD8$^+$ T cell single-cell datasets (**Methods**, **fig. S1b-e**). Seven
82 distinct groups of CD8$^+$ T cells were identified (**fig. 1b-c**); Naïve, central memory (CM), effector
83 memory (EM) and effector cells (ECs) which collectively represent the majority of T cells, as well as
84 highly cycling cells (Mitotic), γδ T cells (gd), and *KLRB1*-expressing mucosal-associated invariant T
85 cells (MAIT), which formed a separate cluster from the rest of the cells. Mitotic cells had higher nUMI
86 detected per cell and a bias towards S and G2M cell cycle phases (**fig. S1f-g**), with a similar expression

87 profile to previous single-cell descriptions of mitotic T cells*(13, 20)*. Expression of *TRDC* was used to
88 identify the gd subset *(21)*, which was enriched for *KLRC3*, *KIR3DL2* and *KIR3DL3* (**fig. 1c**). To
89 distinguish the biological features of each subset, we performed Gene Ontology Biological Pathways
90 (GOBP) enrichment analysis (**fig. 1d**) which highlighted key immune pathways such as *IFNG* signalling
91 and T cell activation selectively enriched in EM and ECs, whilst Naïve/CM and Mitotic subsets were
92 marked by upregulated translational and mitochondrial machinery respectively. Lastly, we examined
93 the expression of T cell activation and exhaustion markers across the cell subsets either as distinct
94 markers (**fig. 1e**) or using co-correlated expression scores (**Methods**, **fig. 1c**). Increased expression of
95 genes associated with T cell exhaustion (*TOX*, *TOX2*, *HAVCR2, LAG3*) resulted in distinct grouping of
96 Mitotic, ECs, EM and gd cells from the remaining subsets. Across the 'conventional' T cell subsets,
97 activation, cytotoxicity and exhaustion all increased towards more differentiated cells, peaking in the
98 ECs. Altogether, we identified highly distinct sub-populations with divergent activation and functional
99 profiles.

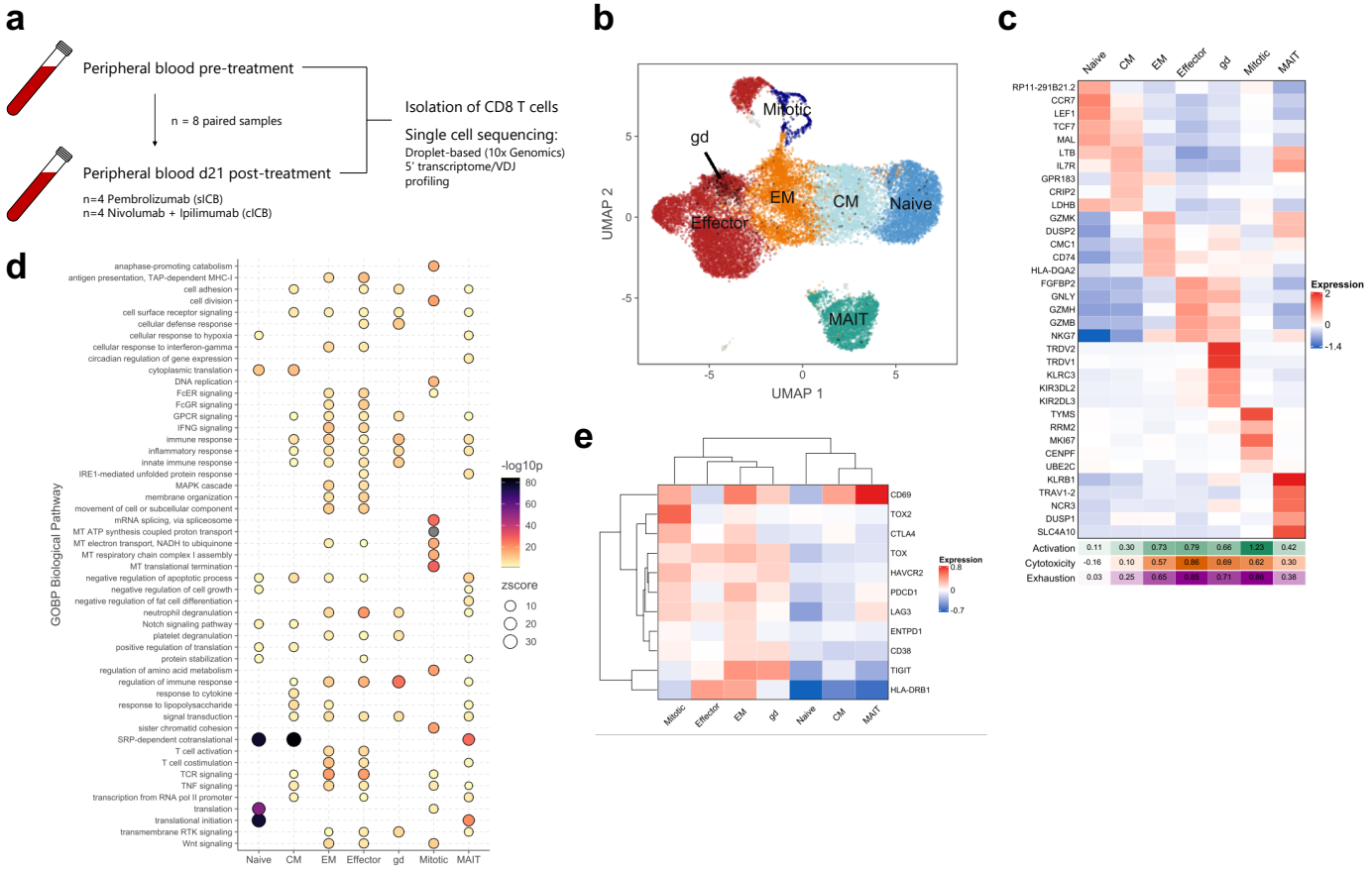

Figure 1: Identification of peripheral CD8^{+} T cell subsets in metastatic melanoma before and during ICB. *(**a**) Workflow for sample collection and processing for single-cell RNAseq. (**b**) UMAP clustering of 22,445 peripheral CD8^{+} T cells from 8 individuals sampled at pre-treatment and following 21 days of ICB, across seven distinct subsets as represented by each colour. (**c**) Expression heatmap showing distinct gene expression profiles and functional scores for the identified subsets. Genes were selected as the top 5 distinguishing genes for each subset at both pre-treatment and at 21d post-ICB. Activation, cytotoxicity and exhaustion scores were calculated for each subset as displayed. (**d**) Dotplot heatmap showing Gene Ontology Biological Process (GOBP) terms significantly enriched across each subset (adjusted p-value<0.05). (**e**) Expression heatmap of selected T cell activation and exhaustion markers.*

110 **Effector CD8$^+$ T cells show increased sensitivity to immune checkpoint blockade**

111 To characterise responses to ICB at a sub-population level we focused on the four 'conventional' T cell
112 subsets of Naïve, CM, EM and ECs. We controlled for increased power to detect differentially
113 expressed (DE) genes in larger subsets by subsampling varying numbers of cells across each subset
114 (analysis bootstrapped 100 times). Across the four subsets, when accounting for increasing numbers of
115 cells sampled, ECs had higher DE gene counts with treatment (**fig. 2a**, **S2a**). The most significantly
116 upregulated genes included markers of maturation (*CD52*), and interferon response (*CD74*, *IFITM3*)
117 (**fig. 2b**). Most of the DE genes in ECs were exclusively modulated in this subset (**fig. S2b**), suggesting
118 a unique effect of ICB on these cells. Subset-wise GOBP analysis of the induced genes demonstrated
119 both conserved biological pathways upregulated across all subsets (**fig. 2c, S2c**), and an additional set
120 of pathways specific to ECs. Pathways commonly induced were ubiquitously expressed across subsets
121 at baseline (**fig. S2d**), unlike those uniquely regulated in EM and ECs, and were enriched in expression
122 in Naïve and CM cells (**fig. S2e**). Pathways restricted to ECs instead encompassed metabolic and
123 immune pathways including NFκB and TNF signalling (**fig. 2d**), further supporting the enhanced
124 stimulatory effect of ICB on this subset.

125 To assess broad changes in T cell function following checkpoint blockade, we examined changes in
126 activation and exhaustion scores across each of the subsets. All subsets showed significant or borderline
127 significant (EM) increases in activation score at C2, whereas cytotoxicity appeared unchanged and
128 exhaustion score increased in the CM and EC subsets (**fig. 2e, S2f**). When we scored cells for both
129 stimulatory and inhibitory pathways induced by ICB*(22)*, we found that *IFNA*-signalling was
130 upregulated post-treatment across all T cell subsets, suggesting extrinsic exposure; whilst IFNγ, PD-1
131 and TCR signalling were more restricted to EM and ECs (**fig. 2f, S2g**). Dissimilar to their relationship
132 with *IFNA* pathways; TCR, PD-1 and IFNγ signalling showed modest/high correlation, reflecting
133 overlapping regulation (**fig. S2h**). These three signalling pathways were most notably induced in EM
134 and EC subsets, with IFNγ signalling being confined to these two sub-populations (**fig. 2f**). Thus, ECs
135 are uniquely responsive to ICB, displaying activation and pro-inflammatory gene expression consistent

with increased TCR ligation, denoted by increases in exhaustion markers, PD-1 signalling and TCR signalling*(22)*.

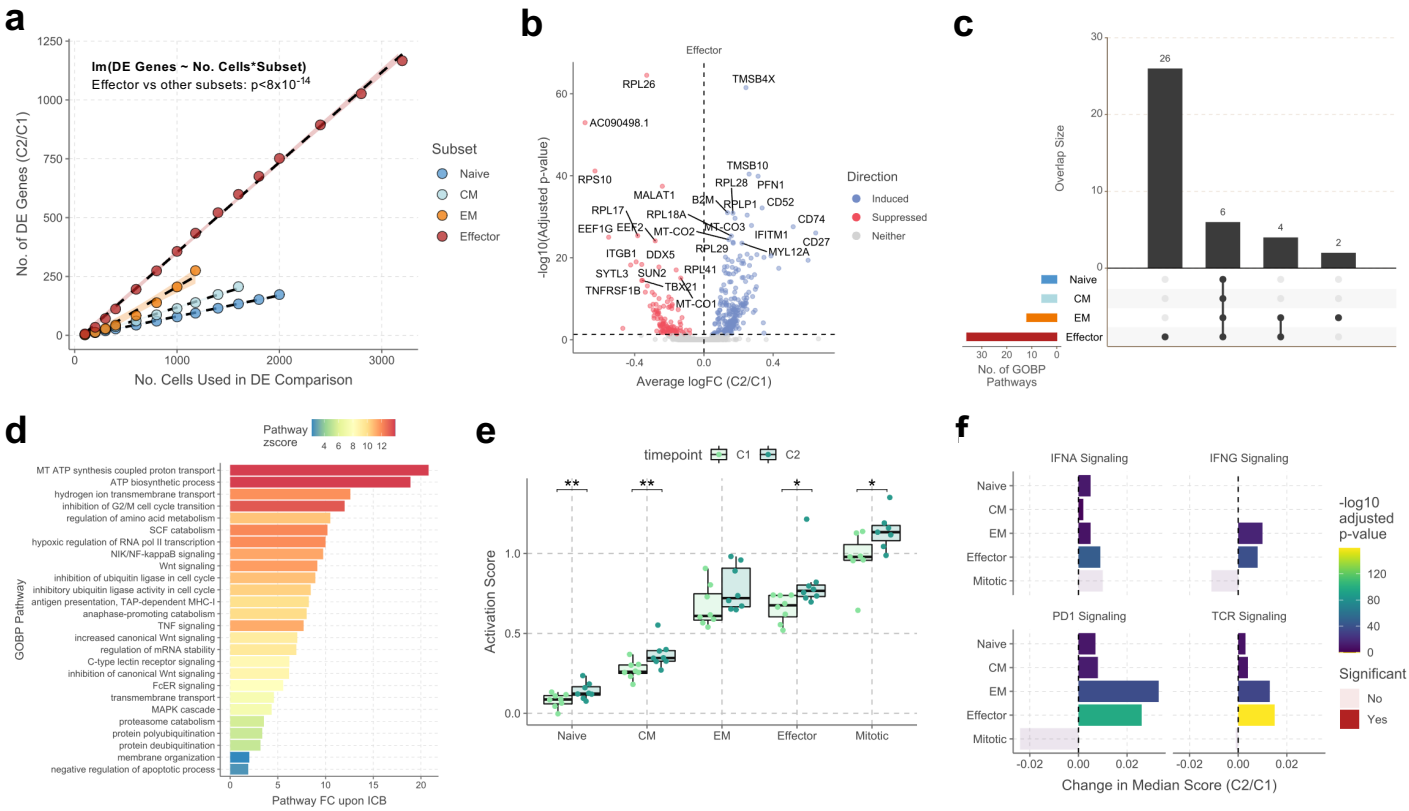

Figure 2: Subset-specific gene expression changes upon ICB. ***(a)*** *Number of differentially expressed (DE) genes (adjusted p-value<0.05) upon ICB for each conventional T cell subset with >300 cells at both timepoints. To control for the distinct numbers of cells in each subset, we subsampled to differing numbers of cells, bootstrapped to 100 iterations. A linear mixed effect model determined differences in the gradients of the slope across all subsets as indicated, with adjusted p-value<8x10^{-14} comparing effector cells and each other subset.* ***(b)*** *Volcano plot of DE genes in ECs upon ICB (adjusted p-value<0.05).* ***(c)*** *Using the maximal number of cells present in all subsets (n=1180), pathway analysis using GOBP was performed on genes upregulated by ICB in each subset; the overlap across each of the pathways visualised using an Upset plot.* ***(d)*** *GOBP pathways uniquely upregulated in effector cells ordered by fold change.* ***(e)*** *Changes in activation score for each subset upon treatment (**Methods**); the*

150 *median score per individual is plotted.* ***(f)*** *Change in AUC scores for selected Reactome pathways*
151 *following ICB across CD8$^+$ T cell subsets (two-sided Wilcoxon-ranked sign test).*

152

153 **ICB leads to a subset specific mitotic response**

154 In parallel to exploring effects on gene expression, we assessed whether ICB treatment changed the
155 relative proportions of these subsets. Across individuals we found ICB significantly reduced CM
156 proportion (**fig. 3a**), whilst other subsets remained relatively unchanged. To explore the generalisability
157 of these findings we developed composite expression signatures for each single-cell subset (**table S2**)
158 and characterised the geometric mean expression of these signatures in bulk RNA-sequencing data
159 isolated in a similar fashion from CD8$^+$ T cells*(16)* (n=220 paired C1/C2 samples from 110 individuals).
160 For almost all single-cell samples, bulk data had been generated, and comparing score-inferred versus
161 known proportions in these two datasets showed that, except for EM, bulk expression scores
162 significantly correlated with single-cell proportions (**fig. S3a**), supporting the validity of this approach.
163 Furthermore, as expected, Naïve and CM scores were anti-correlated with age, whilst EM and EC scores
164 increased with participant age*(23)* (**fig. S3b**). Interestingly, whilst ICB significantly reduced Naïve and
165 CM expression scores, in tandem increasing EM and mitotic scores (**fig. 3b**), no significant change in
166 the EC score was observed, inferring that proportions of ECs remained stable. Correcting for age,
167 mitotic scores demonstrated a weighted increase in cICB compared to sICB treated individuals (**fig.**
168 **S3c-d**), reflecting the stronger effect of cICB on CD8$^+$ T cell responses*(16)*. Finally, the decrease in
169 Naïve and CM score was inversely correlated with mitotic score increase (**fig. S3e**), suggesting ICB
170 elicits shuttling from these subsets into the highly-cycling mitotic pool.

171 To explore differentiation patterns across subsets we employed trajectory analysis*(24, 25)*. Visualisation
172 of the pseudotime map showed a starting state populated with Naïve cells with gradual progression
173 towards CM and EM phenotypes (Branch A), which subsequently bifurcates into effector and mitotic-
174 dominated endpoints (Branch B & C respectively) (**figure 3c, S4a**), implying two alternate fate
175 branches for peripheral CD8$^+$ T cells. As expected, progression along pseudotime was significantly

176 correlated with increasing cell maturity and cytotoxicity (**fig. S4b**). We examined whether changes in
177 pseudotime could be detected upon treatment. Visual examination of pseudotime-ordered cells at C1 vs
178 C2 showed an under-representation of cells in Branch C pre-treatment (**fig. S4c**). Pseudotime
179 significantly increased following ICB, the largest increase occurring when we considered cells in
180 Branch A and C only (**fig. S4d**). Additionally, when we separated cells from each individual amongst
181 the three branches and compared cell proportions between C1 and C2, we found significant increases
182 in the proportion of cells in Branch C, with a concordant decrease in cells located in Branch A (**fig.**
183 **S4e**). This supports the remodelling of the peripheral $CD8^+$ T cell compartment from Naïve/CM cells
184 by ICB, towards a mitotic population within 21 days, with a more marked effect of cICB.

185

186 **Mitotic cells fail to attain cytotoxic markers**

187 Given their marked expansion following ICB, we further characterised the phenotype of the mitotic cell
188 subset. Since they typify the pseudotime end-point state of trajectory Branch C, we examined the key
189 distinctions between the Branch B and Branch C. We clustered genes that significantly associated with
190 pseudotime (adjusted p-value$<1x10^{-4}$) and showed divergent patterns of expression across branches
191 (**fig. S4f**). Consistent with increased proportion of EM and ECs, cytotoxic and early activation genes
192 were enriched in Branch B, whilst markers of proliferation and cell-cycle regulation were associated
193 with Branch C. We assessed pseudotime effect at the subset level by comparing expression for the
194 same subset across branches. EM and ECs from Branch B were comparatively enriched for MHC-I and
195 cytotoxic markers, whilst Branch C EM/ECs showed upregulation of naïve and exhaustion markers
196 including *CD27* and *GZMK(26)*, and translation and metabolic pathways (**fig. S4g-h**). The lack of
197 functional cytotoxicity accrued by mitotic cells was illustrated by projection of various T cell markers
198 onto the pseudotime trajectory (**fig. 3d**), with expression of *IFNG* and the activation-induced
199 transcription factor *EOMES* localised to Branch B. The TCR-signalling associated molecule *CD247*
200 was expressed on most cells except for mitotic cells at the very endpoint of Branch C. Interestingly,
201 *MKI67* expression was limited to terminal cells at both ends of Branch B and C whilst *PDCD1*
202 expression, upregulated post-activation, was enriched across cells in Branch B and to a lesser extent,

203 Branch C. Accordingly, *MKI67* expression on mitotic cells was far in excess of other subsets (**fig. S4i**),
204 reflecting their likely involvement in the ICB-induced proliferative burst*(27, 28)*. Additionally, mitotic
205 cells expressed minimal *CCR7* and had an enrichment of *TIGIT* expression, again concordant with a
206 more terminally exhausted state*(26)*.

207 Using the VDJ sequences we determined clonal relationships between mitotic cells and other sub-
208 populations. Whilst most mitotic compartment cells represented clones restricted to this subset (68% at
209 C1 and 76% at C2), cells from clones common to other subsets were predominantly shared with ECs
210 pre (OR 11.6, $P<1x10^{-10}$, Fisher's test), and post-treatment (OR 1.5, $p < 1.3 x10^{-6}$, Fisher's test, **fig. 3e**).
211 Mitotic clones represented in other cell subsets were typically larger than those that were not (C1;
212 $P<2.9x10^{-9}$, C2; $P<2x10^{-16}$, Kolmogorov-Smirnov test), with a number of clones in the former
213 comprising >0.5% of the repertoire (**fig. 3f**), suggesting a proportion of the mitotic cell compartment is
214 composed of clonally expanded cells. Conversely, when considering *all* clones within the mitotic
215 subset, we found they were on average smaller than their effector counterparts (**fig. 3g**). We further
216 explored this clonal relationship using bulk RNA-sequencing samples, correlating mitotic score with
217 number of expanding clones. Interestingly, baseline mitotic score and subsequent clonal expansion were
218 not associated, whereas C2 mitotic score was highly correlated with expanding clone count (**fig. 3h**),
219 suggesting ICB allows mitotic cells to undergo clonal expansion and switch compartments. In keeping
220 with this, the mitotic score in bulk data significantly anti-correlated with the proportion of clones
221 occupying >0.5% of repertoire at C2 (**fig. S5a**). Thus, whilst the mitotic subset contributes to persistence
222 of established clones, the majority of mitotic cells observed in MM fail to form persistent clones. Thus
223 C1 mitotic cell clones were comparatively less frequently detected at C2 than C1 EC clones, and C2
224 mitotic clones were correspondingly less detected at day 63 or onwards of treatment (C4+) (**fig. 3i**).
225 The disconnect between the mitotic subset and sustained T cell responses is also evidenced by the lack
226 of association between mitotic score, at either pre or post-treatment, with patient outcome, as measured
227 by progression-free survival (PFS) (**fig. 3j**), whilst higher EC score at C2 was associated with
228 significantly longer PFS (**fig. S5b**). Despite this, mitotic score at C4+ remained significantly increased
229 compared to at C1 (**fig. 3k**), indicative of ongoing T cell stimulation across multiple cycles of ICB.

230 Collectively, these findings suggest that Ki67^{+} cells at day 21 post-ICB predominantly represent short-

231 lived cells that do not progress to outcome-associated expanded clones.

232

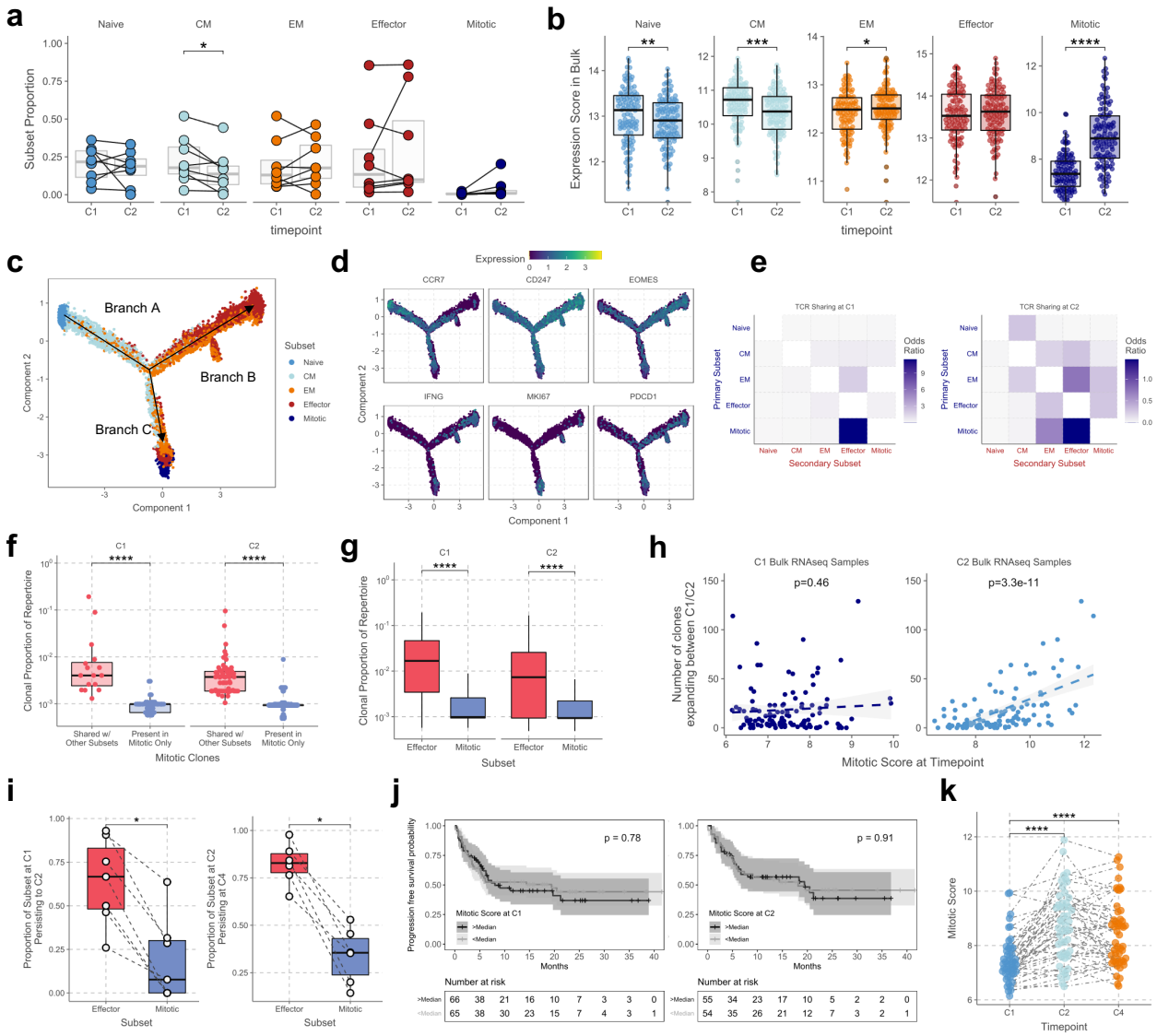

233

234 ***Figure 3**: Dynamic changes in the peripheral CD8^{+} T cell compartment during early ICB. (a-b) (a-*

235 ***b)** Changes in the proportion of each cell subset between pre-treatment (C1) and 21d post-ICB (C2) as*

236 *determined by single-cell RNAseq (n=8, two-sided Wilcoxon-signed rank test) **(a)** or inferred from bulk*

237 *RNAseq data (n=110, two-sided Wilcoxon-signed rank test) **(b)**. For the bulk RNAseq inference, subset*

238 *scores were calculated for each bulk RNAseq sample based on a list of markers that distinguished each*

239 *subset at both pre-treatment and 21d post-ICB in the single-cell RNAseq data (Methods, Extended Data*

240 *Fig. 2a-b).* ***(c)*** *Visualisation of inferred pseudotime trajectories for CD8$^+$ T cells excluding γδ and MAIT*
241 *cells, coloured by subset and arrows indicating increasing pseudotime along three branches (Branches*
242 *A-C).* ***(d)*** *Expression of selected genes along the pseudotime map.* ***(e)*** *Fisher's exact test results showing*
243 *enrichment for overlapping TCR CDR3 sequences between the indicated subsets at C1 (left) and C2*
244 *(right), determined using single-cell RNA/VDJ-seq. Filled boxes represent comparisons between*
245 *subsets that shared significant overlap (adjusted p-value < 0.05).* ***(f)*** *Comparison of clonal sizes of*
246 *mitotic clonotypes that are found across other subsets (n=23 and 77 clones) or solely as mitotic cells*
247 *(n=49 and 244 cells) at C1 and C2 respectively based on single-cell RNA/VDJ-seq (two-sided*
248 *Kolmogorov-Smirnov test).* ***(g)*** *Comparison of clonal sizes of effector cells (n=2537 and 3507 cells)*
249 *and mitotic cells (n=72 and 321 cells) at C1 and C2 respectively based on single-cell RNA/VDJ-seq*
250 *(two-sided Mann Whitney U-test).* ***(h)*** *Pearson's correlation between calculated mitotic score in bulk*
251 *RNAseq samples and the number of expanding TCR clones detected in those samples via MiXCR with*
252 *an adjusted p-value < 0.001, at C1 (left, n=111) and C2 (right, n=111).* ***(i)*** *Proportion of effector and*
253 *mitotic cells that have CDR3 sequences at C1 (left) and C2 (right) that are also detected at C2 and C4*
254 *respectively across each individual (n=7, two-sided Wilcoxon-signed rank test).* ***(j)*** *Kaplan Meier*
255 *curves of progression-free survival according to mitotic score at C1 (left, n=131) or C2 (right, n=109).*
256 ***(k)*** *Changes in mitotic scores at C1 (d0), C2 (d21) or C4 (d63) of treatment (n=49 individuals, two-*
257 *sided Wilcoxon-signed rank test).*

258

259 **CD8$^+$ T cell clones have canonical gene expression associations with clonal size**

260 We have previously shown that patients with more peripheral large clones post-treatment have
261 improved oncological outcome*(16)*. To explore this further we grouped CD8$^+$ T cell clones into five
262 categories based on clonal size as a proportion of the total repertoire (**Table 1**). As expected, most Naïve
263 cells were found in the smallest size categories (**fig. 4a**). Interestingly, EC proportion increased with
264 clone size at C1, whereas the proportion of CM cells decreased (**fig. 4a**). Of note, at C2 there was a
265 higher proportion of EM cells and the greatest proportion of ECs was found in the large and very large
266 size category (>0.5% of the repertoire). As expected, Shannon diversity decreased as clonal size

267 category increased (**fig. 4b**) and when plotted on a UMAP, clones clustered according to size, in
268 accordance with differences in underlying phenotypes (**fig. 4c)**. Larger clones predominantly group
269 within pseudotime Branch B, with higher pseudotime scores, suggesting greater differentiation of $CD8^+$
270 T cells as clonal size increased (**fig. 4d**).

Category	Clonal size (proportion of repertoire)
Very small	< 0.1%
Small	≥ 0.1 < 0.25%
Medium	≥ 0.25 < 0.5%
Large	≥ 0.5 ≤ 2.5%
Very large	≥ 2.5%

271

272 **Table 1**: Clonal size category bins.

273 To further define expression correlates of clone size we performed differential gene expression across
274 bulk RNA-sequencing from 169 individuals (**Methods, fig. 4e**). As per the single-cell data, smaller
275 clones associated with genes of naivety (e.g. *CD27, LEF1*) whilst larger clones expressed markers of
276 cytotoxic maturity such as *FCRL6(29)*. Hierarchical cluster analysis demonstrated smaller clones to be
277 the most dissimilar from others, with further degrees of separation between the medium-sized subsets
278 and the large, notably associated with *PDCD1* expression, and very large clones (**fig. 4e**).

279

280 **ICB differentially affects peripheral $CD8^+$ T cell clones as a function of their size**

281 We next assessed the relationship between clonal size and ICB effect, agnostic to subset type, by
282 performing category-wise differential expression analysis across treatment, using sampling to control
283 for variation in cell number across sub-population and timepoint, with analysis bootstrapped 100 times
284 (**fig. 4f**). This produced a U-shaped response pattern of DE genes according to clone size, with very
285 small clones having a comparatively more DE genes than intermediate-sized clones but fewer than very
286 large clones. We went on to qualitatively analyse the differences in gene expression profile and noted
287 that medium, large and very large clones (0.25-0.5%, 0.5-2.5% and >2.5% of total repertoire) upregulate

288 a number of pro-inflammatory and pro-migratory genes when compared to smaller clones, along with
289 TCR encoding genes, previously shown to associate with clinical outcome*(16)* **(fig. S6**).

290 To further understand these qualitative differences, we analysed GOBP pathways corresponding to the
291 DE genesets (**fig. 4g**). We again noted that large and very large clones had a strikingly divergent gene
292 expression profile following ICB compared to smaller clones, with upregulation of pathways including
293 leukocyte migration, inflammatory response, cell adhesion and adaptive immune response, which were
294 downregulated in very small and small clones. Thus clonal size influences both the magnitude of
295 response to ICB as well as the types of genes regulated, with larger clones displaying marked
296 enhancement of immune function post-treatment.

297

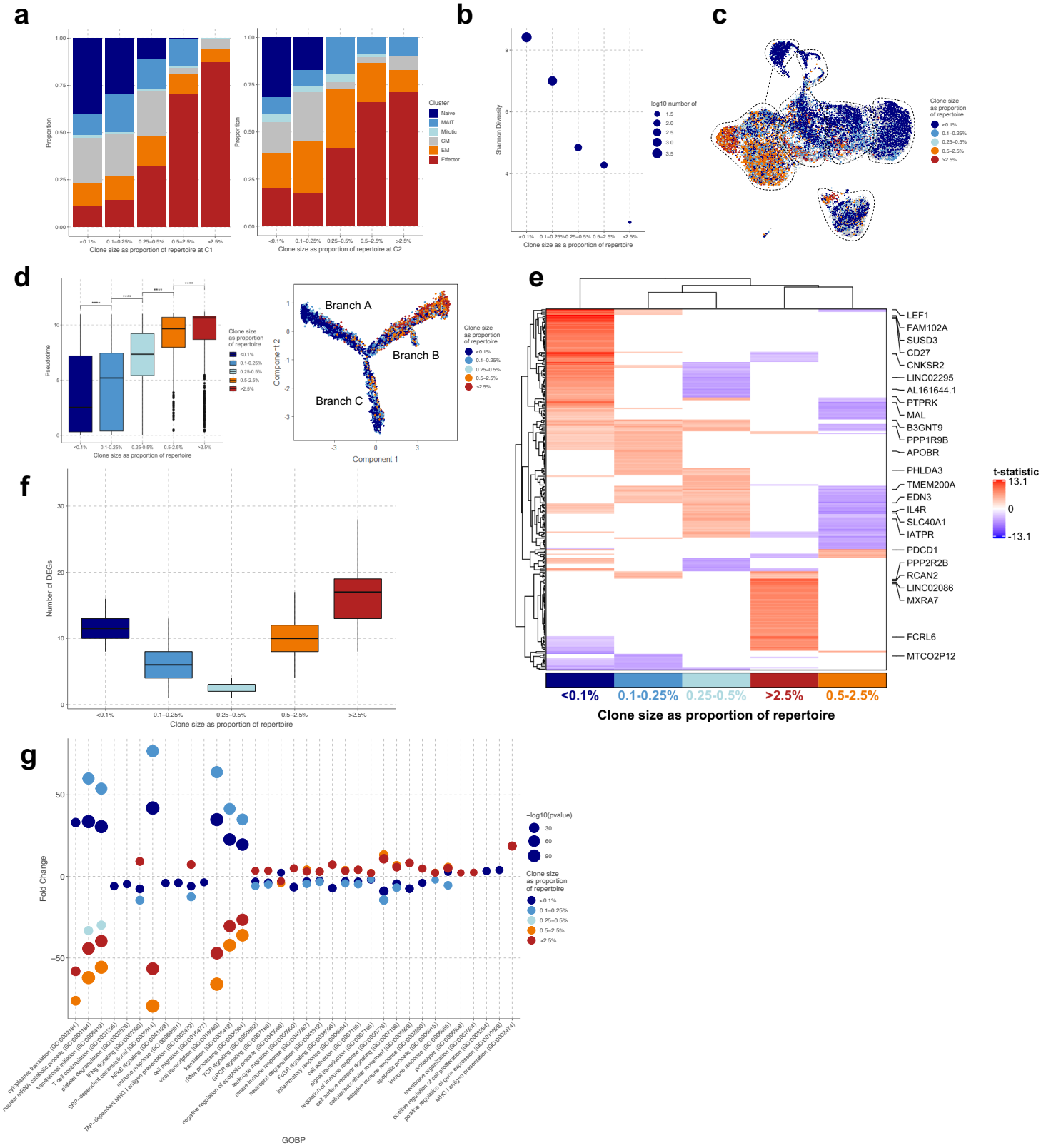

298

299 ***Figure 4: T cell clones have canonical markers, and differentially respond to ICB, as a function of***

300 ***clonal size. (a)*** *Clonal size bins are coloured according to phenotypic cluster at baseline (C1, left) and*

301 *21 days post-treatment (C2, right).* ***(b)*** *Shannon diversity decreases across increasing clonal size*
302 *categories both pre- and post-treatment with ICB.* ***(c)*** *CD8$^+$ T cell clones are binned based on clonal*
303 *size and displayed on a UMAP plot, coloured by clonal size category.* ***(d)*** *Pseudotime scores per clonal*
304 *size category (left) and pseudotime plot coloured per clonal size category (right) demonstrating*
305 *increasing pseudotime as clonal size increases.* ***(e)*** *Heatmap demonstrating canonical gene markers*
306 *that associate with clonal size (n=169 individuals).* ***(f)*** *Number of differentially expressed genes (DEGs)*
307 *pre- and post-ICB for clones of different size categories. Random samples of even size were taken and*
308 *the analysis bootstrapped 100x. There is a statistically significant difference (p<0.001) between all*
309 *groups.* ***(g)*** *Gene Ontology: Biological Pathways analysis for DEGs following ICB treatment in*
310 *different size clone categories.*

311

312 **Cytotoxic clones demonstrate propensity to persist post-ICB treatment**

313 To understand the temporal relationship across the peripheral CD8$^+$ T cell compartment and establish
314 whether cytotoxic T cells are present at baseline, or 'emerge' post-ICB, we divided T cell clones into
315 four categories, namely; (1) clones represented in data from C1 but undetected at C2, (2) those present
316 in the C1 data and resampled at C2, (3) from the perspective of the C2 data, those present at C1, and
317 (4) those uniquely sampled at C2 – 'emergent'. Cytotoxicity scores were calculated for each identified
318 clone. Whilst clones resampled across timepoints were predominantly large or very large **(fig. 5a)**, we
319 found persistent clones consistently displayed higher cytotoxicity scores pre and post-ICB, irrespective
320 of clonal size **(fig. 5b)**. Small emergent C2 clones conversely had lower cytotoxicity than similar-sized
321 persistent clones, whereas large and very large emergent clones had equivalent or higher cytotoxicity
322 scores (**fig. 5a**). Thus clones with higher cytotoxicity pre-treatment have an increased propensity to
323 persist post-ICB. Whilst we did not find ICB increased EC cytotoxicity in the subset based analysis
324 (**fig. S2f**), in keeping with persistence of baseline-cytotoxic clones post-treatment we find that, unlike
325 smaller clones, large clones show increased cytotoxicity with treatment (**fig. S7c**), illustrating clone size
326 induces heterogeneity in the EC response.

327 To investigate the validity of these findings over longer timescales, we examined bulk RNA-sequencing
328 of peripheral $CD8^+$ T cells from the same individuals at 63-106 days post-treatment (C4+, n=6). Within
329 these samples, we were able to identify 992 unique TCRβs associated with 4,245 cells that were present
330 in C2 single-cell samples. Cells from these more durable clones were mainly effector in phenotype, and
331 from large or very large clones (**fig. 5c**). This was similarly the case for the C1 samples, where 880
332 predominant effector phenotype cells were found across 297 clones persisting to C4+ (**fig. S7a**). Thus,
333 persistence was strongly associated with T cell size, with almost 100% of large and very large clones
334 persisting (**fig. 5d, S7b**). Furthermore, clonal size remained closely correlated between C2 and C4+,
335 with very large clones at C2 also being detected as very large clones at C4+ (rho=0.88, $p<2.2x10^{-16}$, **fig.**
336 **5e**), indicating persistence of very large clones is not simply due to resampling probability, but that
337 large clones are maintained for prolonged periods post-ICB.

338 Genes associated with persistence were found to consist of cytotoxic markers (e.g. *CCL4, CCL5, PRF1*)
339 and markers of large clonal size (**fig. S7c**). To delineate between markers of clonal size and persistence,
340 we constrained analysis to non-naïve clones (those >0.1% of the repertoire), and noted that persistent
341 clones were enriched for pro-inflammatory and migratory GOBP pathways, such as TNF/IFNγ
342 signalling, T cell activation, antigen presentation and cellular/subcellular movement (**fig. 5f,g;**
343 **supplementary data 1**). Finally, we examined the baseline phenotype of C4+ persistent clones based
344 on their cytotoxicity score at C1. As per clones persisting to C2, cells from clones that persisting for
345 this longer duration similarly display elevated baseline cytotoxicity across small and medium clone
346 categories (**fig. S7d**). Thus cells from clones persisting post-ICB show increased cytotoxicity before
347 treatment, indicating ICB preferentially enhances pre-existing anti-tumour immunity as opposed to
348 generating a *de novo* response. Using cytotoxicity scores for each individual generated from bulk
349 sequencing data (C1 n=131, C2 n=109) we find a cytotoxicity score above the cohort median construes
350 significantly increased PFS (**fig. 5h**). This was true at both C1 and C2, supporting the finding that
351 baseline immune responses, as well as the enhancement conferred by ICB, is critical in determining
352 clinical outcome.

353

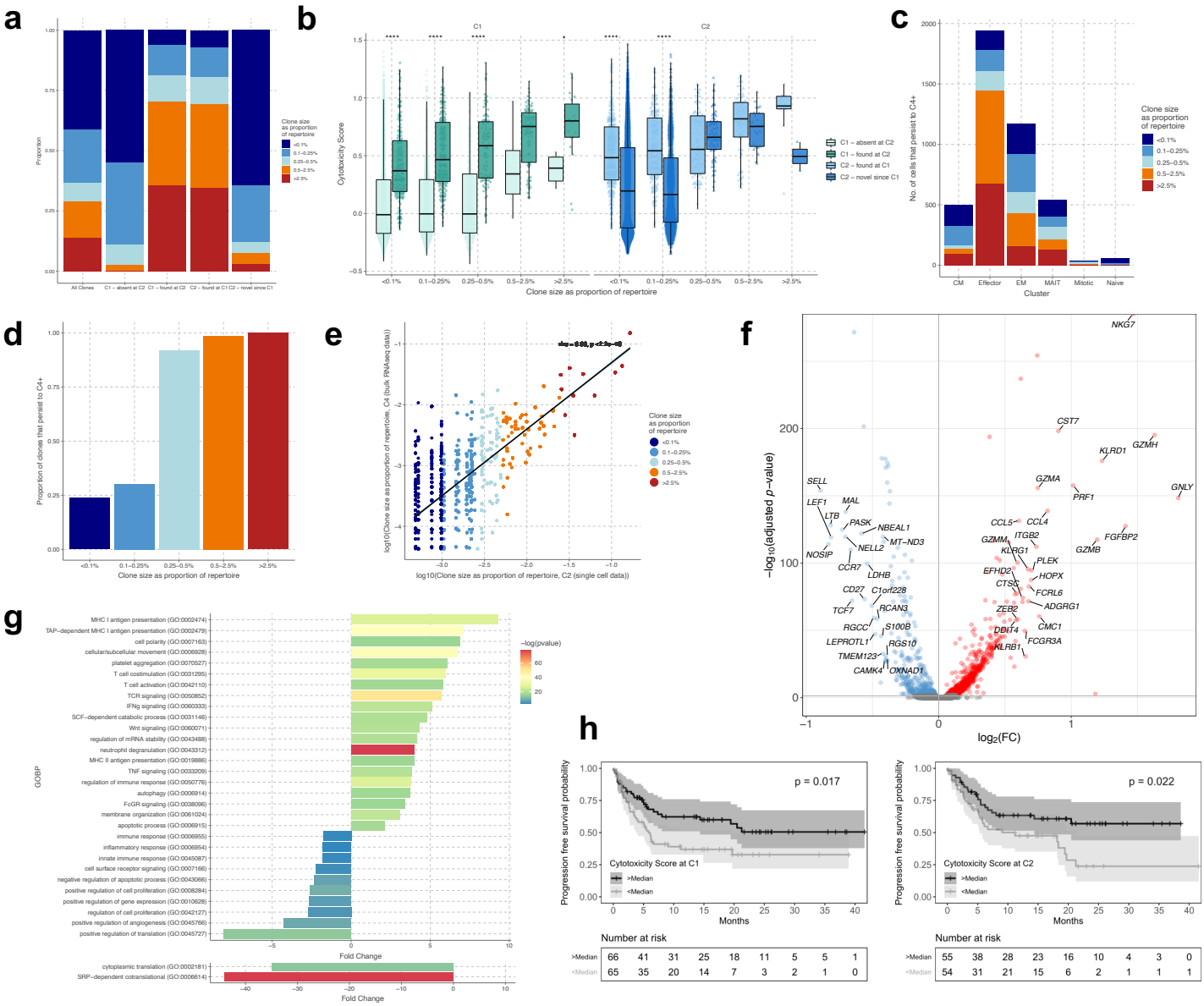

Figure 5: ICB promotes persistence of activated and cytotoxic CD8$^+$ T cells. (a) *CD8$^+$ T cells were classified as to whether they were resampled at both C1 and C2, or whether they were only found at one timepoint. Groups are coloured by binned clonal size as a proportion of total repertoire.* ***(b)*** *Cytotoxicity score of CD8$^+$ T cell clones at baseline (C1, left) or d21 (C2, right). Clones are categorised as to whether they are only sampled at C1 versus if they are resampled at C1 and C2 or if they are found at both timepoints versus if they are novel at C2. Median score per clone is displayed with each point representing a T cell clone. *p<0.05, **p<0.01, ****p<0.0001* ***(c)*** *Clones present in single-cell data at d21 (C2) that can be detected at d63+ (C4+) in bulk RNA-sequencing data, by phenotypic cluster and coloured by clonal size category.* ***(d)*** *Proportion of clones in each size category at C2 that*

363 *can be detected in C4+ in bulk RNA-sequencing data.* ***(e)*** *Size of CD8$^+$ T cell clones at C2 compared*
364 *to the size of the same clone at C4+, coloured by clonal size category.* ***(f)*** *Volcano plot showing*
365 *upregulated (red) or downregulated (blue) genes in cells from very small, small, medium, large or very*
366 *large clones that persist in the peripheral blood to C4+ when compared to those cells from the same*
367 *clonal size categories that do not persist.* ***(g)*** *Pathways (GOBP) that are up- or down-regulated in the*
368 *same cells as in (f).* ***(h)*** *Kaplan-Meier curve showing progression free survival in those patients with*
369 *above median, versus below median, cytotoxicity score at baseline (left) and C2 (right).*

370

371 **ICB drives expansion of large cytotoxic CD8$^+$ T cell clones**

372 Finally, in order to explore CD8$^+$ T cell dynamics with ICB, we focused on cells from clones
373 significantly changing in size following treatment. We identified 44 clones that expand and 56 that
374 contract (**fig. 6a**), with the very large clone category displaying the greatest proportion of expanding
375 and contracting clones (**fig. 6b**). These clones were over-represented amongst those at C2 that persisted
376 to C4+, indicating clones undergoing dynamic change may have greater longevity (**fig 6c**). Whilst we
377 found ICB increased the cytotoxicity score in both expanding and non-expanding clones, expanding
378 clones had higher cytotoxicity at both timepoints (**fig. 6d**), suggesting ICB preferentially drives
379 expansion of more cytotoxic clones.

380 To further corroborate this observation we sought baseline markers of clones that expand following
381 ICB. We identified an enrichment of pro-inflammatory genes, as well as markers associated with tissue
382 trafficking and residency. Interestingly, such clones at baseline over-expressed the transcription factor
383 T-bet (*TBX21)*, and, as per clones that persist, displayed elevated expression of cytotoxic markers
384 including *GNLY, GZMH,* and *CCL5* (**fig. 6e**).

385

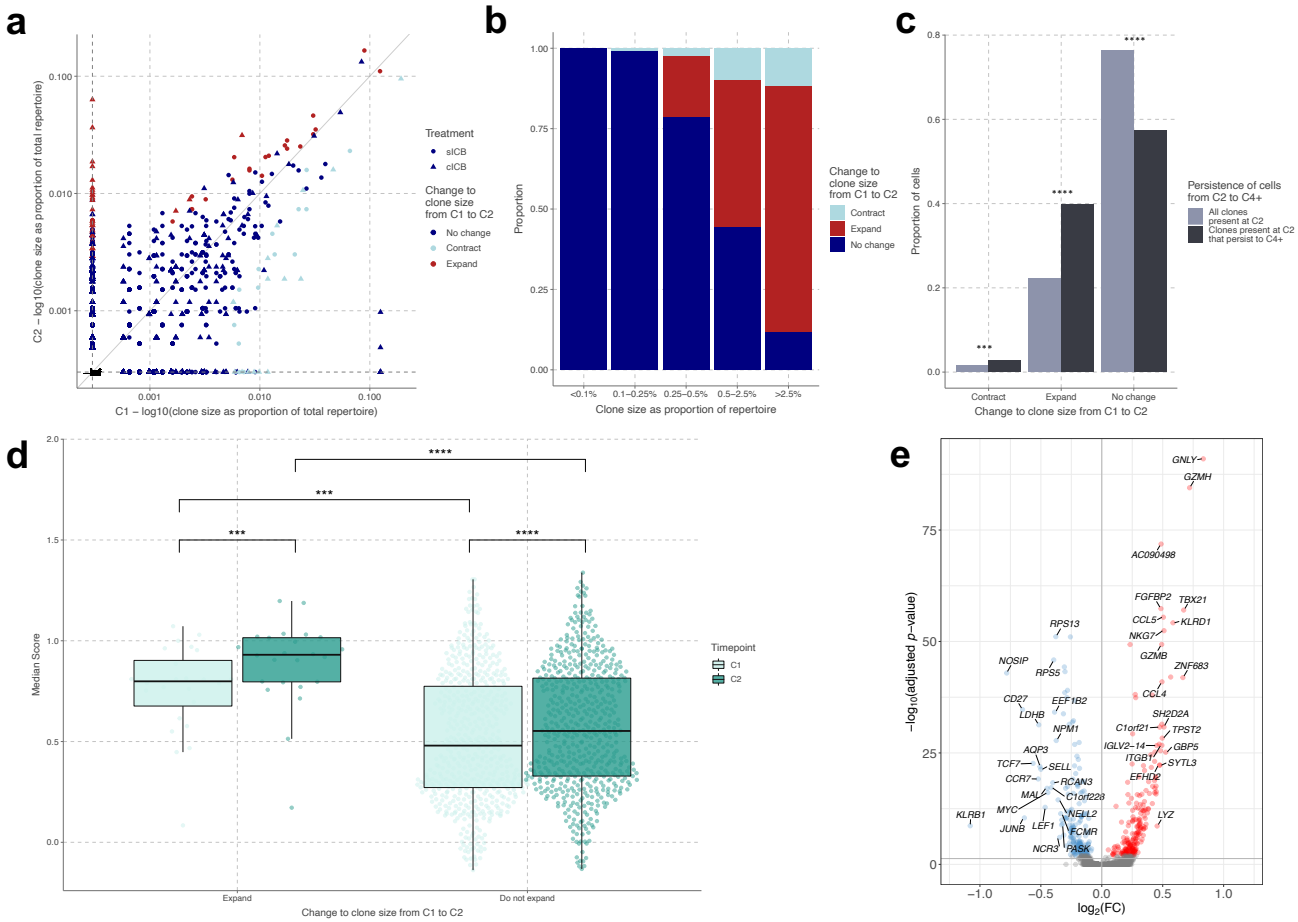

386

387 ***Figure 6: ICB drives expansion of large, cytotoxic CD8$^+$ T cell clones. (a)*** *CD8$^+$ T cell clonal size as*
388 *a proportion of total repertoire at baseline (C1) compared to 21 days post ICB treatment (C2).* ***(b)***
389 *Proportion of each clonal size category coloured by whether a clone has significantly expanded or*
390 *contracted between C1 and C2 of ICB treatment.* ***(c)*** *Proportion of cells that have either expanded,*
391 *contracted or not changed in size between C1 and C2. Light grey columns represent all cells present at*
392 *C2, dark grey columns represent those present at C2 that persist to C4+. ***p < 0.001, ****p<0.0001.*
393 ***(d)*** *Median cytotoxicity score for clones at C1 (light green) and C2 (dark green) depending on whether*
394 *the clone significantly expands or not. ***p < 0.001, ****p<0.0001.* ***(e)*** *Volcano plot showing genes*
395 *at baseline that are upregulated (red) or downregulated (blue) in clones that subsequently expand*
396 *following ICB treatment. Top 30 genes by log_2FC are labelled.*

397

398 **DISCUSSION**

399 Identifying T cell subsets most responsive to ICB is vital in understanding the mechanisms of ICB
400 response and resistance. In this study we have sought to characterise the peripheral $CD8^+$ T cell response
401 to ICB at a single-cell level, characterising responses by sub-populations as well as by clones. We
402 identify seven phenotypic subsets that, as well as sharing a conserved response to ICB, display subset-
403 specific changes, the greatest and most divergent being within the effector cells (ECs). The T effector
404 memory (EM) subset has been described as a crucial mediator in light of its expansion intratumorally
405 and peripherally*(15, 30, 31)*, and we observe increases in the peripheral EM score, inferring
406 commensurate expansion of this subset. We show though that, whilst ICB does not change EC
407 proportion, ECs exhibit the greatest magnitude and most relevant changes post-ICB. Further, the EC
408 compartment preferentially persists following ICB. As such, we posit that in peripheral blood, the
409 effector T cell compartment is most sensitive to ICB treatment. In keeping with this, recent work shows
410 that clones common to blood and tumour are enriched for effector markers and are not exhausted in
411 patients who respond to ICB*(14)*.

412 We find cells undergoing mitosis form a mixed-population of cells, with a proportionally higher clonal
413 overlap with ECs counter-balanced by the majority of mitotic cells not belonging to established clones.
414 In addition to having higher nUMI and increased cell cycle activity, mitotic cells had high exhaustion
415 scores and only moderate levels of cytotoxicity. The use of bulk sequencing data from CD8+ T cells
416 from up to 169 MM patients provided appropriate power to test observations from the scRNA-seq data.
417 Crucially, this demonstrated post-treatment mitotic cell counts were inversely correlated with large
418 clone proportion, indicating that increased peripheral mitotic cells denotes failure to establish large
419 cytotoxic clones, and that it is the cytotoxic as opposed to mitotic response to ICB that dictates
420 outcomes. Of interest, cells from this mitotic sub-population clustered at the end of branch C of the
421 pseudotime trajectory, suggesting inability to establish differentiated progeny is common to most cells
422 within this branch and, instead of progressing to cytotoxic states, these cells remain exhausted and fail
423 to persist. It is important to note that our analysis was at day 21 post commencing treatment and mitotic

events will likely fluctuate across cycles of treatment although, given the half-life of ICB is >21 days, cells will be exposed throughout.

That ICB is found to preferentially affect large clones reveals mechanistic underpinnings to our previous observations linking number of large peripheral T cells with clinical outcomes*(16)*. Smaller clones downregulate expression of immunological pathways and increase expression of ribosomal genes and translational activity post-ICB; whereas, consistent with the observation that translational suppression occurs in terminal effector T cells, larger clones have an opposite response*(32)*.

The observation that ICB promotes survival and expansion of clones that display markers of cytotoxicity *prior* to treatment was supported by the inclusion of late bulk-sequencing data which highlighted that cytotoxic clones persist across multiple cycles of ICB and that baseline cytotoxicity was associated with clinical outcome. That these persistent $CD8^+$ T cells have already attained cytotoxicity pre-treatment indicates ICB leads to promotion of clone survival. The increased response in clones showing baseline cytotoxicity supports the major bottlenecks in response to ICB to be centred on the lack of tumour immunogenicity and antigen presentation, with consequential insufficient effector T cell activation*(33)*. This implies therapeutics targeted at overcoming further immune checkpoints may lead to diminishing clinical returns, whereas future approaches focussed on effective antigen presentation and priming may be more fruitful.

In summary, our work combines in-depth analysis of responses to ICB at the single-cell level with observations corroborated in a large dataset to provide a unique insight into peripheral effects of ICB on $CD8^+$ T cells. The use of V(D)J sequencing allows us to track clones over time, determining that most mitotic cells fail to expand into differentiated large effector clones. Instead, clone size plays a key role in determining the magnitude and nature of response to ICB, and we find the effector subset is most sensitive to treatment. Finally, we reveal that cytotoxic clones have successfully expanded to form persistent subsets – and that much of the effect of ICB appears to rely upon this pre-existent response, highlighting failure of immune recognition as being the major limiter of response to ICB.

450 **MATERIALS AND METHODS**

451 **Sample collection**

452 Patients provided written informed consent to donate samples to the Oxford Radcliffe Biobank (Oxford
453 Centre for Histopathology Research ethical approval nos. 16/A019, 18/A064, 19/A114); 30 – 50 ml
454 blood was collected into EDTA tubes (BD vacutainer system) taken immediately pre-treatment at d0
455 and d21 following one cycle of treatment. Peripheral blood mononuclear cells were obtained by density
456 centrifugation (Ficoll Paque). $CD8^+$ cell isolation was carried out by positive selection (Miltenyi)
457 according to the manufacturer's instructions, with all steps performed either at 4 °C or on ice. Unless
458 otherwise stated, patients receiving cICB (ipilimumab plus nivolumab, n=4) or sICB (pembrolizumab,
459 n=4) were pooled for the purposes of analysis, based on previous work showing qualitatively similar
460 genetic changes induced in peripheral $CD8^+$ T cells by both cICB and sICB*(16)*.

461 **Single-cell sample preparation and sequencing**

462 Magnetically separated $CD8^+$ cells were immediately oil-partitioned into single-cell droplets, followed
463 by cell lysis and a reverse transcription reaction using the 10x Genomics Chromium system. 6000 $CD8^+$
464 T cells were loaded onto each partitioning cassette. Single-cell 5' RNA transcriptome and V(D)J
465 Libraries were constructed from the cDNA, according to the manufacturer's instructions
466 (https://www.10xgenomics.com/). Sequencing was performed on an Illumina HiSeq4000; 75bp PE
467 reads for the 5' RNA libraries, 150 bp PE reads for the V(D)J libraries to a depth of approximately
468 50000 reads per cell.

469 **Data processing, quality control and clustering**

470 Single-cell reads were aligned, counted and filtered for initial quality control (QC) as previously
471 described*(12)*. In short, FASTQ files were generated from Illumina BCL outputs, used to produce gene
472 expression and barcoding libraries, and then combined using the Cellranger *mkfastq*, *count* and *aggr*
473 functions respectively. For V(D)J data, Cellranger *vdj* was applied. For QC, the R package *scater(34)*
474 was used to identify single-cell outliers as low-quality libraries and *scran* utilised to detect doublets
475 which were removed from analysis. Following alignment and data pre-processing, $CD8^+$ T cells were

476 filtered on detectable *CD3D* and either *CD8A* or *CD8B* UMIs whilst lacking *CD14* expression. The R
477 package *Seurat(35)* was used for further QC, data normalisation and identification of variable features;
478 low quality cells were excluded if they had less than 500 total UMIs, less than 300 detected features
479 and mitochondrial gene percentage above 20%. Genes expressed in <5 cells were also removed. The
480 percentage of mitochondrial genes, total nUMIs and cell cycle scores were regressed out upon scaling
481 of the normalised data. Principal component analysis (PCA) was performed on the scaled data and the
482 top 16 principal components selected for dimensionality reduction and UMAP clustering as the most
483 variable and biologically informative components. To determine an ideal resolution value, cell clusters
484 generated using values between 0.1 and 2.5 were compared using the R package *clustree(36)* with
485 values between 1.5 and 2.0 showing high cluster stability.

486 **Identification of cell subsets**

487 To assign each cell cluster generated in Seurat to a functional T cell subset, we curated transcripts per
488 million (TPM) normalised counts for $CD8^+$ T cells from previous T cell cancer scRNAseq datasets*(12,*
489 *13, 37–39)*. Using the R package *SingleR(40)*, each individual cell was matched to one of the $CD8^+$ T
490 cell subsets present in the reference datasets based on global gene expression similarity, from which
491 subset identity for each cluster was determined.

492 **Clonal definitions, size change and diversity**

493 T cell chains were filtered based on called productivity, and chain identity (TRA or TRB). Cells were
494 selected as those that either contained a single TCRβ chain, a combination of one TCRα with one TCRβ
495 chain or a group of three chains – two TCRα and TCRβ. A clone ID was defined by a concatenation of
496 amino acid CDR3 chains present, with cells sharing identical clone IDs classed as members of the same
497 clonotype. Clonal proportions were calculated by dividing the number of cells in each clone per sample
498 by the total of number of cells per sample. Clones were designated to be expanding/contracting if the
499 counts of that clone were greater/less than expected by chance post treatment ($P<0.05$, Fisher's exact
500 test). Shannon diversity was calculated from count data of clones per sample using the R package
501 *entropy(41)*.

502 **Downstream expression analysis**

503 ***Differential gene expression analysis with subsampling.*** Differential gene expression was performed
504 in *Seurat* for all detected genes using the FindMarkers function. Where specified, to control for
505 differences in statistical power in detecting DE genes across groups with varying cell counts, the number
506 of cells used for analysis was standardised to the number present in the smallest group and bootstrapped
507 100 times to account for sampling bias. For comparison of ICB effect according to clone size 245 cells
508 were used as this was the minimum number of cells across categories/timepoints.

509 ***Pathway analysis.*** Pathway enrichment analysis was performed using the R package *XGR(42)* with the
510 GOBP database. Significantly induced or suppressed genes were assessed separately against a
511 background of all detected genes using a hypergeometric test with a minimum overlap set to 8 (figures
512 4, 5) or 10 (figure 2), ontology algorithm specified as 'elimination' and an elimination p value of 0.01.

513 ***Generation of cell phenotype and pathway scores.*** Scores for cell activation, cytotoxicity, exhaustion
514 and maturation were calculated for each individual cell using the AddModuleScore function in Seurat.
515 The top 50 genes that significantly correlated with *CD38, IFNG*, *HAVCR2* and *CD52* expression
516 respectively and were identified as variable features in Seurat were grouped to form gene sets for each
517 score. Each gene set was then used as an input to generate phenotype scores. Cell scores for GOBP and
518 Reactome pathways were generated using the R package *AUCell(43)*, based on the genes in each
519 pathway that were also detected by single-cell RNAseq.

520 ***Pseudotime analysis.*** Pseudotime trajectories were constructed using the R package *monocle(44),*
521 excluding cells assigned gamma-delta or MAIT identity due to their distinct developmental pathways.
522 Cells were downsampled to only those that contained both an alpha and beta CDR3 sequence in the
523 corresponding VDJ-seq due to memory constraints. To identify genes significantly associated with
524 changes in pseudotime, the BEAM test in monocle was performed and genes with qval scores less than
525 $1x10^{-4}$ considered significant.

526 **Bulk RNA-sequencing**

527 Analysis of bulk RNA-sequencing was performed on $CD8^+$ T cells from 169 individuals receiving ICB
528 for MM. For paired analysis of subset scores we used samples with both day 0 and day 21 expression
529 (n=110). For full methods please see*(16)*. Data can be downloaded from the European Bioinformatics
530 Institute and the Centre for Genomic Regulation under accession no. EGAS00001004081.

531 ***Generation of subset and cytotoxicity scores from bulk RNA-sequencing samples.*** Genes with
532 expression significantly enriched in a given subset above all others were identified using the
533 FindAllMarkers function in Seurat across all cells from C1 and C2 samples separately. To minimise
534 timepoint-specific gene expression associations, the top 20 genes at each timepoint were compared and
535 the overlapping genes retained to identify robust subset-specific genes. Subset scores were then
536 generated for each bulk RNAseq sample by first normalising expression data using the *DESeq2* R
537 package*(45)* and then calculating the geometric mean of expression across each list of subset genes. A
538 similar approach was used for cytotoxic score but instead based on the top 50 genes used for single-cell
539 cytotoxic scoring (Data file S2). Out of 136 C1 and 113 C2 samples, 110 individuals had paired C1/C2
540 data with a further 49 having C4 samples. Clinical follow-up was available for 131 C1 and 109 C2
541 samples.

542 ***Identification of clonal category-associated genes.*** To identify genes significantly associated with each
543 clonal category, samples with greater than 1,000 detected TCR-beta chains by MiXCR*(46)* (allowing
544 for detection of clones representing <0.1% of the TCR repertoire) were counted for the number of clones
545 belonging in the five clonal bins based on β-chain CDR3 sequence. In total, 169 individuals were used
546 for analysis across 63 healthy individuals and 106 MM patients. Genes were tested for significance in
547 *DESeq2* using a binomial Wald test with 750 iterations after correcting for size factors and dispersion.
548 For clonal persistence at later timepoints (C4+) we used samples from four individuals taken at day 63,
549 one at day 84 and one at day 106. Clones were defined within these samples using MiXCR according
550 to the beta chain, and then compared with earlier scRNA-seq data with matching beta chain usage.

551 ***Correlating mitotic score with clonal expansion.*** Clones identified using MiXCR from bulk RNA-
552 sequencing data were tracked between C1 and C2. Clones were designated to be expanding if the counts

553 of that clone were greater than expected by chance post treatment (P<0.001, Fisher's exact test). This
554 created a number of expanding clones per sample which was correlated with mitotic score, with
555 overlapping metrics available for 111 individuals.

556 **General statistical analysis**

557 Statistical comparisons were performed as indicated in each figure and conducted in R. Where indicated
558 (by n=7), cells and statistics from donor 6 were excluded due to low numbers of cells at C1. For analysis
559 of clonal persistence, n=6 as only six out of the eight individuals profiled had samples at C4+. All
560 statistical tests were performed in R or *rstatix,* and *lme4*/*lmerTest* for linear effect models. Gene
561 correlation analysis for phenotype scores was performed using *DGCA(47)*. Survival analysis was
562 performed using *survival*/*survminer*. For all data, *p<0.05, **p<0.01, ***p< 0.001, ****p<0.0001.
563 Adjusted p-values have been reported using Bonferroni correction for multiple comparisons.

564

565 **LIST OF SUPPLEMENTARY MATERIALS**

566 Figure S1: Workflow for $CD8^+$ T cell subset assignments

567 Figure S2: Differential gene expression upon ICB in $CD8^+$ T cell subsets

568 Figure S3: Inference of subset proportions in bulk RNAseq data using single-cell expression profiles

569 Figure S4: Pseudotime analysis of $CD8^+$ T cells

570 Figure S5: Subset score associations with clonal and clinical characteristics.

571 Figure S6: Differentially expressed genes across clonal categories

572 Figure S7: Clones present in peripheral blood at day 63+ are more cytotoxic and activated at baseline
573 and day 21

574 Table S1: Donor characteristics and cell count per sample

575 Table S2: Genes for bulk scores

576 Data file S1: CSV file containing differentially expressed genes between large CD8+ T cell clones that
577 persist following ICB and those that do not persist

578 Data file S2: CSV file containing lists of genes use to generate activation, exhaustion and cytotoxicity
579 scores

580 **REFERENCES**

581 1. M. A. Postow, M. K. Callahan, J. D. Wolchok, Immune Checkpoint Blockade in Cancer Therapy.,
582 *Journal of clinical oncology : official journal of the American Society of Clinical Oncology* **33**, 1974–82
583 (2015).

584 2. J. Larkin, V. Chiarion-Sileni, R. Gonzalez, J.-J. Grob, P. Rutkowski, C. D. Lao, C. L. Cowey, D.
585 Schadendorf, J. Wagstaff, R. Dummer, P. F. Ferrucci, M. Smylie, D. Hogg, A. Hill, I. Márquez-Rodas, J.
586 Haanen, M. Guidoboni, M. Maio, P. Schöffski, M. S. Carlino, C. Lebbé, G. McArthur, P. A. Ascierto, G.
587 A. Daniels, G. v. Long, L. Bastholt, J. I. Rizzo, A. Balogh, A. Moshyk, F. S. Hodi, J. D. Wolchok, Five-Year
588 Survival with Combined Nivolumab and Ipilimumab in Advanced Melanoma, *New England Journal of*
589 *Medicine* **381**, 1535–1546 (2019).

590 3. A. M. Goodman, S. Kato, L. Bazhenova, S. P. Patel, G. M. Frampton, V. Miller, P. J. Stephens, G. A.
591 Daniels, R. Kurzrock, Tumor mutational burden as an independent predictor of response to
592 immunotherapy in diverse cancers, *Molecular Cancer Therapeutics* **16**, 2598–2608 (2017).

593 4. J. Y. Kim, A. Kronbichler, M. Eisenhut, S. H. Hong, H. J. van der Vliet, J. Kang, J. il Shin, G. Gamerith,
594 Tumor mutational burden and efficacy of immune checkpoint inhibitors: A systematic review and
595 meta-analysis, *Cancers* **11**, 11 (2019).

596 5. T. A. Chan, M. Yarchoan, E. Jaffee, C. Swanton, S. A. Quezada, A. Stenzinger, S. Peters,
597 Development of tumor mutation burden as an immunotherapy biomarker: Utility for the oncology
598 clinic*Annals of Oncology* **30**, 44–56 (2019).

599 6. T. A. Barnes, E. Amir, HYPE or HOPE: The prognostic value of infiltrating immune cells in
600 cancer*British Journal of Cancer* **117**, 451–460 (2017).

601 7. F. Maibach, H. Sadozai, S. M. Seyed Jafari, R. E. Hunger, M. Schenk, Tumor-Infiltrating
602 Lymphocytes and Their Prognostic Value in Cutaneous Melanoma*Frontiers in Immunology* **11** (2020),
603 doi:10.3389/fimmu.2020.02105.

604 8. A. Castro, R. M. Pyke, X. Zhang, W. K. Thompson, C. P. Day, L. B. Alexandrov, M. Zanetti, H. Carter,
605 Strength of immune selection in tumors varies with sex and age, *Nature Communications* **11** (2020),
606 doi:10.1038/s41467-020-17981-0.

607 9. A. C. Huang, M. A. Postow, R. J. Orlowski, R. Mick, B. Bengsch, S. Manne, W. Xu, S. Harmon, J. R.
608 Giles, B. Wenz, M. Adamow, D. Kuk, K. S. Panageas, C. Carrera, P. Wong, F. Quagliarello, B.
609 Wubbenhorst, K. D'Andrea, K. E. Pauken, R. S. Herati, R. P. Staupe, J. M. Schenkel, S. McGettigan, S.
610 Kothari, S. M. George, R. H. Vonderheide, R. K. Amaravadi, G. C. Karakousis, L. M. Schuchter, X. Xu, K.
611 L. Nathanson, J. D. Wolchok, T. C. Gangadhar, E. J. Wherry, T-cell invigoration to tumour burden ratio
612 associated with anti-PD-1 response, *Nature* **545**, 60–65 (2017).

613 10. N. E. Thomas, K. J. Busam, L. From, A. Kricker, B. K. Armstrong, H. Anton-Culver, S. B. Gruber, R. P.
614 Gallagher, R. Zanetti, S. Rosso, T. Dwyer, A. Venn, P. A. Kanetsky, P. A. Groben, H. Hao, I. Orlow, A. S.
615 Reiner, L. Luo, S. Paine, D. W. Ollila, H. Wilcox, C. B. Begg, M. Berwick, Tumor-infiltrating lymphocyte
616 grade in primary melanomas is independently associated with melanoma-specific survival in the
617 population-based genes, environment and melanoma study, *Journal of Clinical Oncology* **31**, 4252–
618 4259 (2013).

619 11. P. C. Tumeh, C. L. Harview, J. H. Yearley, I. P. Shintaku, E. J. M. Taylor, L. Robert, B. Chmielowski,
620 M. Spasic, G. Henry, V. Ciobanu, A. N. West, M. Carmona, C. Kivork, E. Seja, G. Cherry, A. J. Gutierrez,
621 T. R. Grogan, C. Mateus, G. Tomasic, J. A. Glaspy, R. O. Emerson, H. Robins, R. H. Pierce, D. A.

622 Elashoff, C. Robert, A. Ribas, PD-1 blockade induces responses by inhibiting adaptive immune
623 resistance., *Nature* **515**, 568–71 (2014).

624 12. K. E. Yost, A. T. Satpathy, D. K. Wells, Y. Qi, C. Wang, R. Kageyama, K. L. McNamara, J. M. Granja,
625 K. Y. Sarin, R. A. Brown, R. K. Gupta, C. Curtis, S. L. Bucktrout, M. M. Davis, A. L. S. Chang, H. Y. Chang,
626 Clonal replacement of tumor-specific T cells following PD-1 blockade, *Nature Medicine* **25**, 1251–
627 1259 (2019).

628 13. T. D. Wu, S. Madireddi, P. E. de Almeida, R. Banchereau, Y. J. J. Chen, A. S. Chitre, E. Y. Chiang, H.
629 Iftikhar, W. E. O'Gorman, A. Au-Yeung, C. Takahashi, L. D. Goldstein, C. Poon, S. Keerthivasan, D. E.
630 de Almeida Nagata, X. Du, H. M. Lee, K. L. Banta, S. Mariathasan, M. das Thakur, M. A. Huseni, M.
631 Ballinger, I. Estay, P. Caplazi, Z. Modrusan, L. Delamarre, I. Mellman, R. Bourgon, J. L. Grogan,
632 Peripheral T cell expansion predicts tumour infiltration and clinical response, *Nature* **579**, 274–278
633 (2020).

634 14. L. Lucca, P.-P. Axisa, B. Lu, B. Harnett, S. Jessel, L. Zhang, K. Raddassi, L. Zhang, K. Olino, J. Clune,
635 M. Singer, D. A. Hafler, Circulating Clonally Expanded T Cells Reflect Functions of Tumor Infiltrating T
636 Cells 2 3 Running title 1 Single-cell RNAseq of circulating TILs in Melanoma 2 3, *bioRxiv* ,
637 2020.09.30.321240 (2020).

638 15. S. Valpione, E. Galvani, J. Tweedy, P. A. Mundra, A. Banyard, P. Middlehurst, J. Barry, S. Mills, Z.
639 Salih, J. Weightman, A. Gupta, G. Gremel, F. Baenke, N. Dhomen, P. C. Lorigan, R. Marais, Immune
640 awakening revealed by peripheral T cell dynamics after one cycle of immunotherapy, *Nature Cancer*
641 **1**, 210–221 (2020).

642 16. B. P. Fairfax, C. A. Taylor, R. A. Watson, I. Nassiri, S. Danielli, H. Fang, E. A. Mahé, R. Cooper, V.
643 Woodcock, Z. Traill, M. H. Al-Mossawi, J. C. Knight, P. Klenerman, M. Payne, M. R. Middleton,
644 Peripheral CD8+ T cell characteristics associated with durable responses to immune checkpoint
645 blockade in patients with metastatic melanoma*Nature Medicine* **26**, 193–199 (2020).

646 17. K. H. Kim, J. Cho, B. M. Ku, J. Koh, J. M. Sun, S. H. Lee, J. S. Ahn, J. Cheon, Y. J. Min, S. H. Park, K.
647 Park, M. J. Ahn, E. C. Shin, The first-week proliferative response of peripheral blood PD-1þCD8þ T
648 cells predicts the response to Anti-PD-1 therapy in solid tumors, *Clinical Cancer Research* **25**, 2144–
649 2154 (2019).

650 18. M. Ayers, J. Lunceford, M. Nebozhyn, E. Murphy, A. Loboda, D. R. Kaufman, A. Albright, J. D.
651 Cheng, S. P. Kang, V. Shankaran, S. A. Piha-Paul, J. Yearley, T. Y. Seiwert, A. Ribas, T. K. McClanahan,
652 IFN-γ-related mRNA profile predicts clinical response to PD-1 blockade, *Journal of Clinical*
653 *Investigation* **127**, 2930–2940 (2017).

654 19. P. A. Szabo, H. M. Levitin, M. Miron, M. E. Snyder, T. Senda, J. Yuan, Y. L. Cheng, E. C. Bush, P.
655 Dogra, P. Thapa, D. L. Farber, P. A. Sims, Single-cell transcriptomics of human T cells reveals tissue
656 and activation signatures in health and disease, *Nature Communications* **10**, 1–16 (2019).

657 20. G. X. Y. Zheng, J. M. Terry, P. Belgrader, P. Ryvkin, Z. W. Bent, R. Wilson, S. B. Ziraldo, T. D.
658 Wheeler, G. P. McDermott, J. Zhu, M. T. Gregory, J. Shuga, L. Montesclaros, J. G. Underwood, D. A.
659 Masquelier, S. Y. Nishimura, M. Schnall-Levin, P. W. Wyatt, C. M. Hindson, R. Bharadwaj, A. Wong, K.
660 D. Ness, L. W. Beppu, H. J. Deeg, C. McFarland, K. R. Loeb, W. J. Valente, N. G. Ericson, E. A. Stevens,
661 J. P. Radich, T. S. Mikkelsen, B. J. Hindson, J. H. Bielas, Massively parallel digital transcriptional
662 profiling of single cells, *Nature Communications* **8** (2017), doi:10.1038/ncomms14049.

21. G. Pizzolato, H. Kaminski, M. Tosolini, D. M. Franchini, F. Pont, F. Martins, C. Valle, D. Labourdette, S. Cadot, A. Quillet-Mary, M. Poupot, C. Laurent, L. Ysebaert, S. Meraviglia, F. Dieli, P. Merville, P. Milpied, J. Déchanet-Merville, J. J. Fournié, Single-cell RNA sequencing unveils the shared and the distinct cytotoxic hallmarks of human TCRVδ1 and TCRVδ2 γδ T lymphocytes, *Proceedings of the National Academy of Sciences of the United States of America* **116**, 11906–11915 (2019).

22. A. Ribas, J. D. Wolchok, Cancer immunotherapy using checkpoint blockade*Science* **359**, 1350–1355 (2018).

23. R. Aguirre-Gamboa, I. Joosten, P. C. M. Urbano, R. G. van der Molen, E. van Rijssen, B. van Cranenbroek, M. Oosting, S. Smeekens, M. Jaeger, M. Zorro, S. Withoff, A. E. van Herwaarden, F. C. G. J. Sweep, R. T. Netea, M. A. Swertz, L. Franke, R. J. Xavier, L. A. B. Joosten, M. G. Netea, C. Wijmenga, V. Kumar, Y. Li, H. J. P. M. Koenen, Differential Effects of Environmental and Genetic Factors on T and B Cell Immune Traits, *Cell Reports* **17**, 2474–2487 (2016).

24. C. Trapnell, D. Cacchiarelli, J. Grimsby, P. Pokharel, S. Li, M. Morse, N. J. Lennon, K. J. Livak, T. S. Mikkelsen, J. L. Rinn, The dynamics and regulators of cell fate decisions are revealed by pseudotemporal ordering of single cells, *Nature Biotechnology* **32**, 381–386 (2014).

25. X. Qiu, Q. Mao, Y. Tang, L. Wang, R. Chawla, H. A. Pliner, C. Trapnell, Reversed graph embedding resolves complex single-cell trajectories, *Nature Methods* **14**, 979–982 (2017).

26. G. Galletti, G. de Simone, E. M. C. Mazza, S. Puccio, C. Mezzanotte, T. M. Bi, A. N. Davydov, M. Metsger, E. Scamardella, G. Alvisi, F. de Paoli, V. Zanon, A. Scarpa, B. Camisa, F. S. Colombo, A. Anselmo, C. Peano, S. Polletti, D. Mavilio, L. Gattinoni, S. K. Boi, B. A. Youngblood, R. E. Jones, D. M. Baird, E. Gostick, S. Llewellyn-Lacey, K. Ladell, D. A. Price, D. M. Chudakov, E. W. Newell, M. Casucci, E. Lugli, Two subsets of stem-like CD8+ memory T cell progenitors with distinct fate commitments in humans, *Nature Immunology* (2020), doi:10.1038/s41590-020-0791-5.

27. A. C. Huang, M. A. Postow, R. J. Orlowski, R. Mick, B. Bengsch, S. Manne, W. Xu, S. Harmon, J. R. Giles, B. Wenz, M. Adamow, D. Kuk, K. S. Panageas, C. Carrera, P. Wong, F. Quagliarello, B. Wubbenhorst, K. D'Andrea, K. E. Pauken, R. S. Herati, R. P. Staupe, J. M. Schenkel, S. McGettigan, S. Kothari, S. M. George, R. H. Vonderheide, R. K. Amaravadi, G. C. Karakousis, L. M. Schuchter, X. Xu, K. L. Nathanson, J. D. Wolchok, T. C. Gangadhar, E. J. Wherry, T-cell invigoration to tumour burden ratio associated with anti-PD-1 response, *Nature* **545**, 60–65 (2017).

28. S. J. Im, M. Hashimoto, M. Y. Gerner, J. Lee, H. T. Kissick, M. C. Burger, Q. Shan, J. S. Hale, J. Lee, T. H. Nasti, A. H. Sharpe, G. J. Freeman, R. N. Germain, H. I. Nakaya, H. H. Xue, R. Ahmed, Defining CD8+ T cells that provide the proliferative burst after PD-1 therapy, *Nature* **537**, 417–421 (2016).

29. D. M. Schreeder, J. Pan, F. J. Li, E. Vivier, R. S. Davis, FCRL6 distinguishes mature cytotoxic lymphocytes and is upregulated in patients with B-cell chronic lymphocytic leukemia, *European Journal of Immunology* **38**, 3159–3166 (2008).

30. A. Ribas, D. S. Shin, J. Zaretsky, J. Frederiksen, A. Cornish, E. Avramis, E. Seja, C. Kivork, J. Siebert, P. Kaplan-Lefko, X. Wang, B. Chmielowski, J. A. Glaspy, P. C. Tumeh, T. Chodon, D. Pe'er, B. Comin-Anduix, PD-1 blockade expands intratumoral memory T cells, *Cancer Immunology Research* **4**, 194–203 (2016).

31. M. Enamorado, S. Iborra, E. Priego, F. J. Cueto, J. A. Quintana, S. Martýnez-Cano, E. Mejyás-Perez, M. Esteban, I. Melero, A. Hidalgo, D. Sancho, Enhanced anti-tumour immunity requires the interplay between resident and circulating memory CD8+ T cells, *Nature Communications* **8**, 1–11 (2017).

705 32. K. Araki, M. Morita, A. G. Bederman, B. T. Konieczny, H. T. Kissick, N. Sonenberg, R. Ahmed,
706 Translation is actively regulated during the differentiation of CD8 + effector T cells, *Nature*
707 *Immunology* **18**, 1046–1057 (2017).

708 33. R. W. Jenkins, D. A. Barbie, K. T. Flaherty, Mechanisms of resistance to immune checkpoint
709 inhibitors, *British Journal of Cancer* **118**, 9–16 (2018).

710 34. D. J. McCarthy, K. R. Campbell, A. T. L. Lun, Q. F. Wills, Scater: Pre-processing, quality control,
711 normalization and visualization of single-cell RNA-seq data in R, *Bioinformatics* **33**, 1179–1186
712 (2017).

713 35. A. Butler, P. Hoffman, P. Smibert, E. Papalexi, R. Satija, Integrating single-cell transcriptomic data
714 across different conditions, technologies, and species, *Nature Biotechnology* **36**, 411–420 (2018).

715 36. L. Zappia, A. Oshlack, Clustering trees: a visualization for evaluating clusterings at multiple
716 resolutions, *GigaScience* **7** (2018), doi:10.1093/gigascience/giy083.

717 37. X. Guo, Y. Zhang, L. Zheng, C. Zheng, J. Song, Q. Zhang, B. Kang, Z. Liu, L. Jin, R. Xing, R. Gao, L.
718 Zhang, M. Dong, X. Hu, X. Ren, D. Kirchhoff, H. G. Roider, T. Yan, Z. Zhang, Global characterization of
719 T cells in non-small-cell lung cancer by single-cell sequencing, *Nature Medicine* **24**, 978–985 (2018).

720 38. P. Savas, B. Virassamy, C. Ye, A. Salim, C. P. Mintoff, F. Caramia, R. Salgado, D. J. Byrne, Z. L. Teo,
721 S. Dushyanthen, A. Byrne, L. Wein, S. J. Luen, C. Poliness, S. S. Nightingale, A. S. Skandarajah, D. E.
722 Gyorki, C. M. Thornton, P. A. Beavis, S. B. Fox, P. K. Darcy, T. P. Speed, L. K. MacKay, P. J. Neeson, S.
723 Loi, Single-cell profiling of breast cancer T cells reveals a tissue-resident memory subset associated
724 with improved prognosis, *Nature Medicine* **24**, 986–993 (2018).

725 39. L. Zhang, X. Yu, L. Zheng, Y. Zhang, Y. Li, Q. Fang, R. Gao, B. Kang, Q. Zhang, J. Y. Huang, H. Konno,
726 X. Guo, Y. Ye, S. Gao, S. Wang, X. Hu, X. Ren, Z. Shen, W. Ouyang, Z. Zhang, Lineage tracking reveals
727 dynamic relationships of T cells in colorectal cancer, *Nature* **564**, 268–272 (2018).

728 40. D. Aran, A. P. Looney, L. Liu, E. Wu, V. Fong, A. Hsu, S. Chak, R. P. Naikawadi, P. J. Wolters, A. R.
729 Abate, A. J. Butte, M. Bhattacharya, Reference-based analysis of lung single-cell sequencing reveals a
730 transitional profibrotic macrophage, *Nature Immunology* **20**, 163–172 (2019).

731 41. J. Hausser, K. Strimmer, Entropy inference and the james-stein estimator, with application to
732 nonlinear gene association networks, *Journal of Machine Learning Research* **10**, 1469–1484 (2009).

733 42. H. Fang, B. Knezevic, K. L. Burnham, J. C. Knight, XGR software for enhanced interpretation of
734 genomic summary data, illustrated by application to immunological traits, *Genome Medicine* **8**, 129
735 (2016).

736 43. S. Aibar, C. B. González-Blas, T. Moerman, V. A. Huynh-Thu, H. Imrichova, G. Hulselmans, F.
737 Rambow, J. C. Marine, P. Geurts, J. Aerts, J. van den Oord, Z. K. Atak, J. Wouters, S. Aerts, SCENIC:
738 Single-cell regulatory network inference and clustering, *Nature Methods* **14**, 1083–1086 (2017).

739 44. C. Trapnell, D. Cacchiarelli, J. Grimsby, P. Pokharel, S. Li, M. Morse, N. J. Lennon, K. J. Livak, T. S.
740 Mikkelsen, J. L. Rinn, The dynamics and regulators of cell fate decisions are revealed by
741 pseudotemporal ordering of single cells, *Nature Biotechnology* **32**, 381–386 (2014).

742 45. M. I. Love, W. Huber, S. Anders, Moderated estimation of fold change and dispersion for RNA-
743 seq data with DESeq2, *Genome Biology* **15** (2014), doi:10.1186/s13059-014-0550-8.

46. D. A. Bolotin, S. Poslavsky, I. Mitrophanov, M. Shugay, I. Z. Mamedov, E. v. Putintseva, D. M. Chudakov, MiXCR: Software for comprehensive adaptive immunity profiling*Nature Methods* **12**, 380–381 (2015).

47. A. T. McKenzie, I. Katsyv, W. M. Song, M. Wang, B. Zhang, DGCA: A comprehensive R package for Differential Gene Correlation Analysis, *BMC Systems Biology* **10** (2016), doi:10.1186/s12918-016-0349-1.

751 **ACKNOWLEDGEMENTS**

752 We are very grateful to all patients who generously contributed samples and participated in the study.
753 We thank all the staff of the Day Treatment Unit, Oxford Cancer Centre, and The Brodey Centre at the
754 Horton General Hospital. We also thank M. Payne, N. Coupe and R. Matin for assistance in collecting
755 patient samples. We thank M. H. Al-Mossawi for discussion and advice.

756 **FUNDING**

757 This study was funded by a Wellcome Intermediate Clinical Fellowship to BPF (no. 201488/Z/16/Z),
758 additionally supporting AV, EAM and IN. RAW was a National Institute for Health Research (NIHR)
759 Academic Clinical Fellow at the time of this project, and was supported by a Cancer Research UK
760 (CRUK) predoctoral Fellowship (no. ANR00740); currently funded by a Wellcome Trust Doctoral
761 Training Fellowship (no. BST00070). OT is supported by The Clarendon Fund, St Edmund Hall, and
762 an Oxford Australia Scholarship. RC is supported by a CRUK Clinical Research Training Fellowship.
763 CAT is funded by the Engineering & Physical Sciences Research Council and the Balliol Jowett Society
764 (no. D4T00070). MRM and BPF are supported by the NIHR Oxford Biomedical Research Centre. The
765 views expressed are those of the authors and not necessarily those of the NHS, the NIHR or the
766 Department of Health.

767 **AUTHOR CONTRIBUTIONS**

768 RAW & BPF conceived the study; RAW, OT, IN & BPF performed the analysis, figures were generated
769 by OT & RAW, manuscript was drafted by RAW, OT & BPF; RAW & RC performed single-cell
770 experiments; RAW, EAM, RC, CAT, AV & OT collected and prepared samples, MRM contributed to
771 discussions throughout the work; BPF oversaw the project. All authors read, edited and approved the
772 final manuscript.

773 **COMPETING INTERESTS**

774 RAW, OT, RC, CAT, AV, EAM, IN – no competing interests

MRM – reports grants from Roche, grants from Astrazeneca, grants and personal fees from GSK, personal fees and other from Novartis, other from Millenium, personal fees and other from Immunocore, personal fees and other from BMS, personal fees and other from Eisai, other from Pfizer, personal fees, non-financial support and other from Merck/MSD, personal fees and other from Rigontec (acquired by MSD), other from Regeneron, personal fees and other from BiolineRx, personal fees and other from Array Biopharma (now Pfizer), non-financial support and other from Replimune, personal fees from Kineta, personal fees from Silicon Therapeutics, outside the submitted work.

BPF – received conference support from BMS.

DATA AND MATERIALS AVAILABILITY

Raw expression matrices and associated cell metadata for all cells that passed upstream QC will be deposited on EGA. All scripts used in data analysis and the generation of figures will be made available on the Fairfax group bitbucket account.

SUPPLEMENTARY MATERIALS

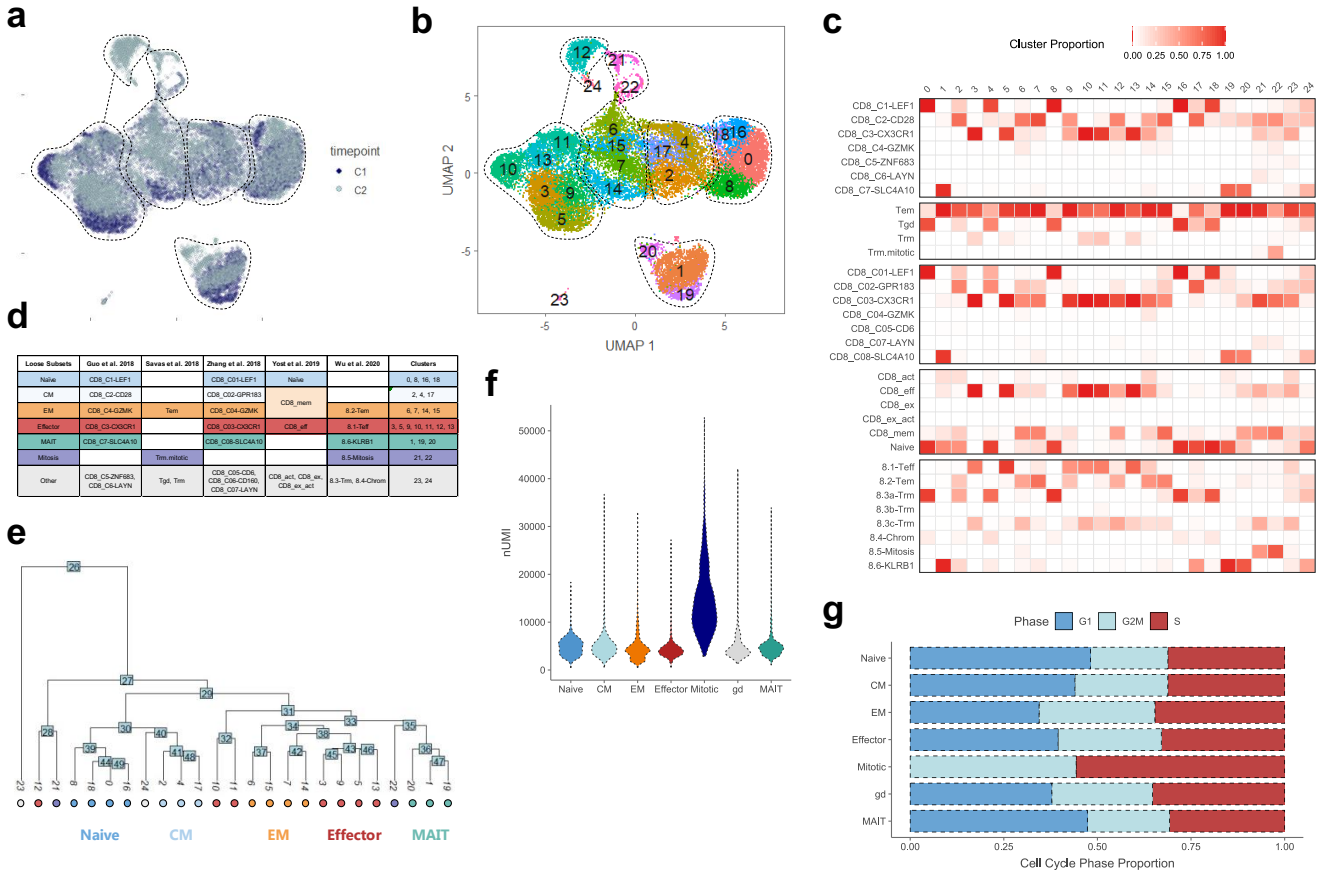

***Figure S1**: **Workflow for CD8$^+$ T cell subset assignments.** **(a)** UMAP distribution of cells from pre-treatment (C1) and day 21 on-treatment (C2) samples. **(b)** UMAP visualisation of 25 Seurat clusters generated at a FindClusters resolution of 1.5. **(c)** Heatmap of assigned subset identities for each Seurat cluster using external cancer patient single-cell RNAseq datasets as a reference (refs). For each cell, SingleR was used to cross-match its expression profile to that of one of the subsets in each reference set. The proportion of cells in each cluster that were assigned a particular identity from each reference set is represented by the intensity of shading (between 0 and 1). **(d)** Summary table of subset identities for each reference set and assigned identities for each cluster based on the best match from the SingleR analysis. **(e)** Phylogenetic tree for each Seurat cluster coloured by assigned subset showing similarity between clusters within the same subset. **(f)** Violin plot showing the nUMI per cell across each of the seven CD8$^+$ T cell subsets. **(g)** Bar plot of the proportion of cells in each stage of the cell cycle, assigned using the CellCycleScoring function in Seurat, across each subset.*

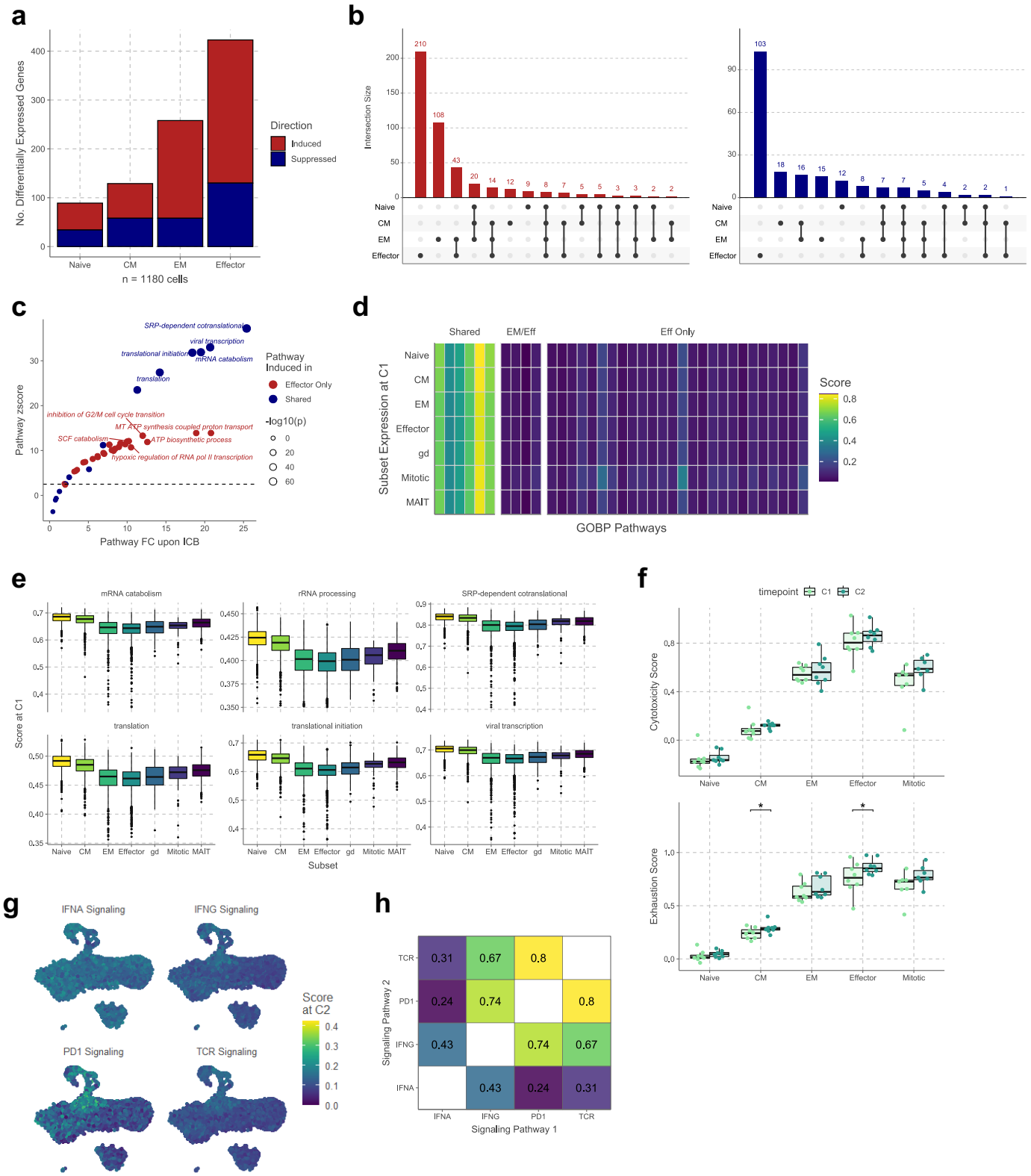

***Figure S2**: **Differential gene expression upon ICB in CD8$^+$ T cell subsets.** **(a)** Summary of the number of differentially expressed genes modulated by ICB for each subset at n=1180 cells. **(b)** Upset plot for overlapping significantly induced (left) and suppressed (right) genes across each subset. **(c)** GOBP*

804 *pathways upregulated by ICB in effector cells coloured based on whether they were uniquely induced*
805 *in effector cells or also upregulated across other CD8$^+$ T cell subsets (adjusted p-value < 0.05).* ***(d)***
806 *Pathway AUC scores at pre-treatment (C1) for all induced pathways across all T cell subsets, separated*
807 *based on the patterns of overlap.* ***(e)*** *AUC scores for pathways commonly induced in all T cell subsets*
808 *across all T cell populations.* ***(f)*** *Changes in cytotoxicity and exhaustion score for each subset upon*
809 *treatment. Scores were calculated using the AddModuleScore function in Seurat using a list of the top*
810 *50 genes with expression correlated with that of IFNG and HAVCR2 respectively, and the median score*
811 *per individual plotted (n=8, two-sided Wilcoxon-ranked sign test).* ***(g)*** *Overlay of AUC scores on cell*
812 *UMAP at d21 post-treatment (C2) for selected Reactome pathways.* ***(h)*** *Pearson's correlation values*
813 *for AUC scores of Reactome pathways across all C2 cells.*

814

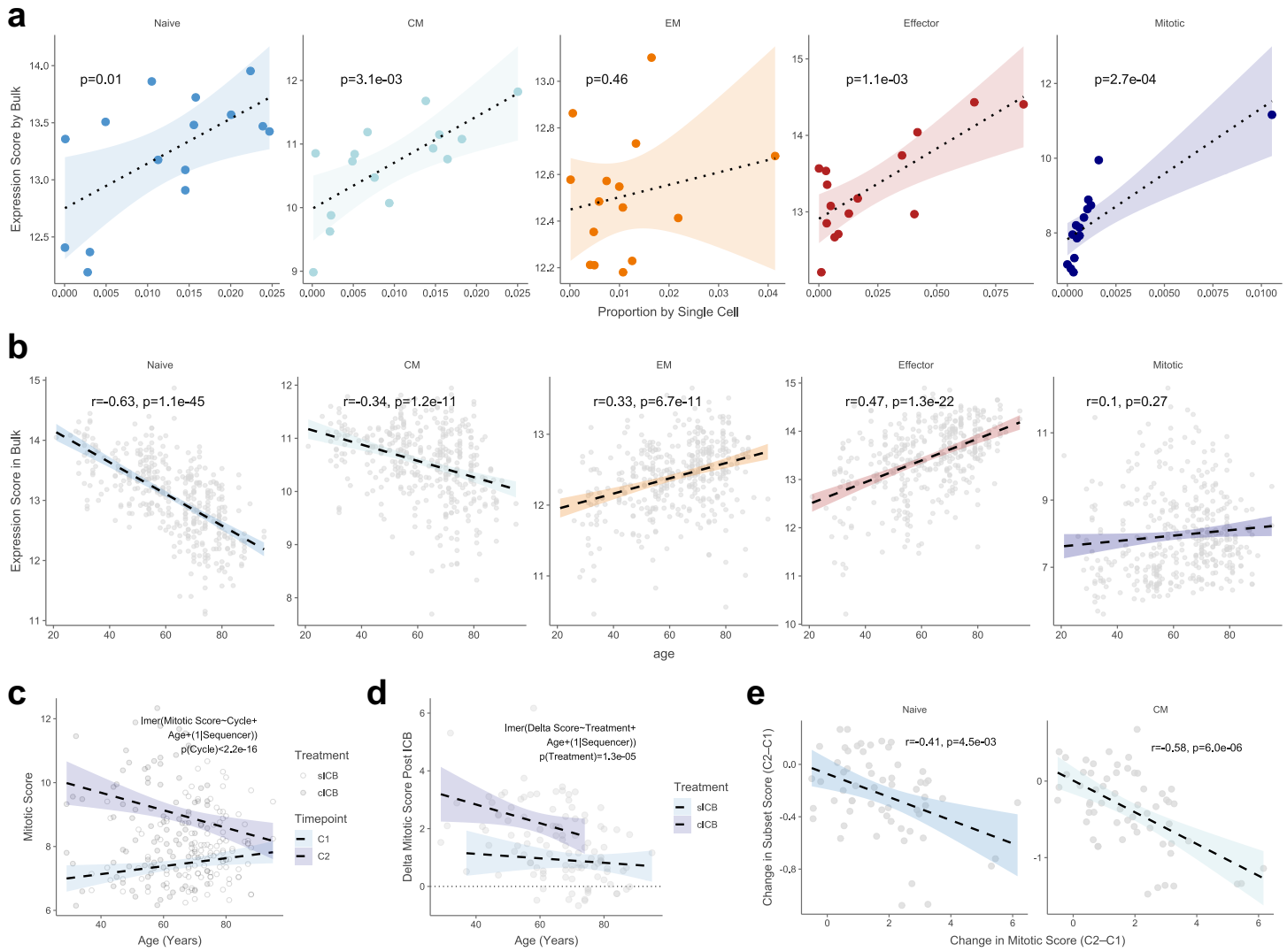

Figure S3**: **Inference of subset proportions in bulk RNAseq data using single-cell expression profiles. (a)** Concordance plot between subset proportions for each single-cell sample and scores calculated for each subset using bulk RNAseq data of CD8$^+$ T cells. For 15/16 of the samples used for single-cell RNAseq, bulk RNAseq on the purified CD8$^+$ T cells was also performed. A list of the top 20 discriminating markers for each subset was generated using FindAllMarkers in the single-cell data for all pre-treatment cells, and separately for all cells at d21 post-ICB. The overlapping genes were retained as markers of each cell subset irrespective of treatment, and the geometric mean expression for each set of genes was calculated using normalised bulk RNAseq data, thus generating subset scores for each bulk RNAseq sample. Pearson's correlation was used to determine the accuracy of this scoring approach for each subset, showing good concordance for all subsets except effector memory (EM). **(b)

826 *As a further validation of the bulk RNAseq scores, subset scores across n=399 samples were correlated*
827 *against participant age using Pearson's correlation.* ***(c)*** *Linear mixed effect model for mitotic score*
828 *showing a significant increase in score following ICB upon controlling for age and fitting sequencing*
829 *run as a random effect (n=110 individuals).* ***(d)*** *Linear mixed effect model for change in mitotic score*
830 *following ICB showing a significantly higher change in patients treated with combination ICB*
831 *compared to single-agent ICB, controlling for age and fitting sequencing run as a random effect (n=110*
832 *individuals).* ***(e)*** *Pearson's correlation between changes in mitotic score upon ICB, and corresponding*
833 *changes in Naïve score (left) and CM score (right) per individual (n=110).*

834

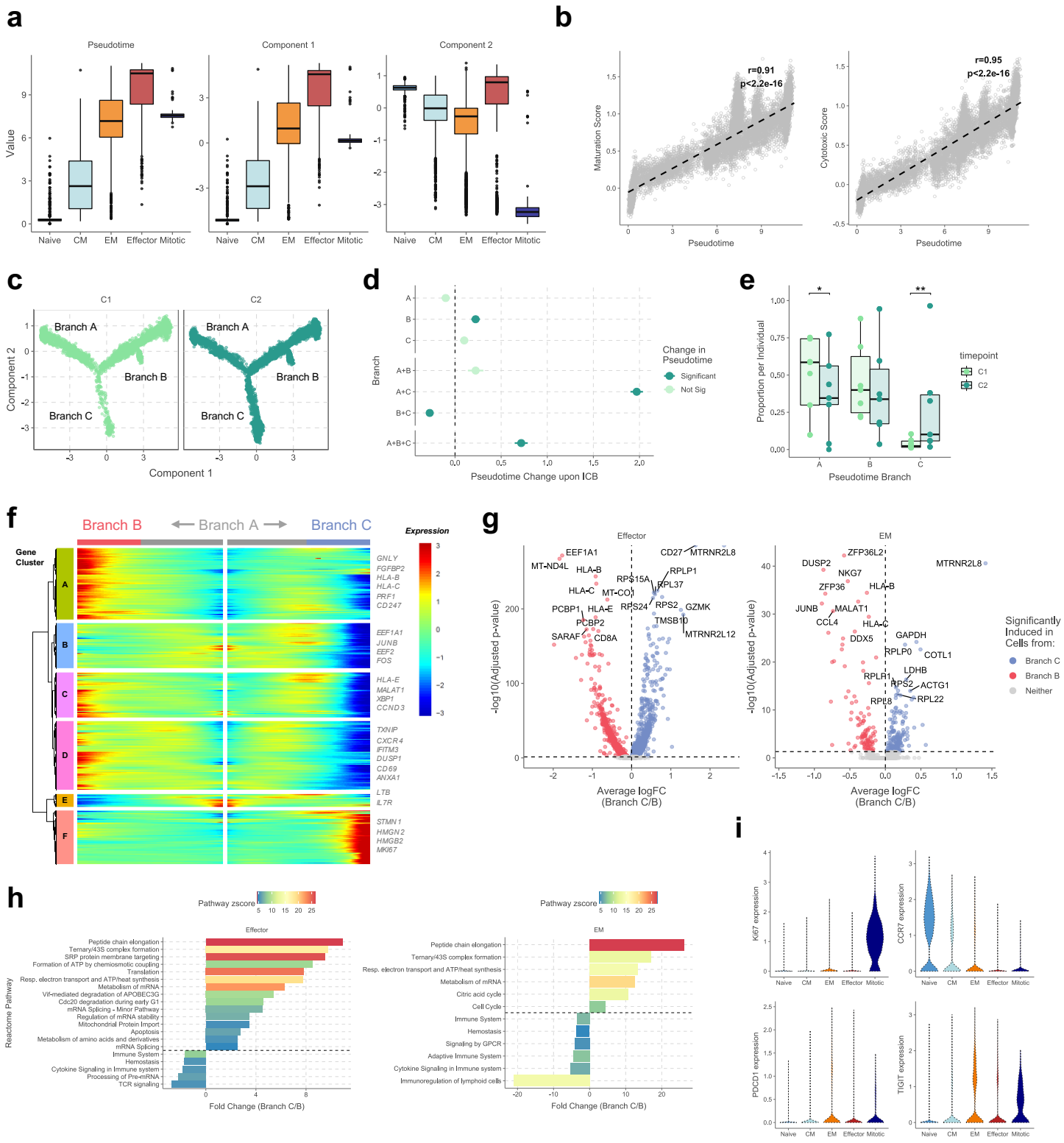

***Figure S4*: Pseudotime analysis of CD8⁺ T cells. (a)** *Pseudotime and trajectory component values generated using Monocle across each conventional CD8⁺ T cell subset.* **(b)** *Pearson's correlation*

838 *between pseudotime values per cell, and maturation and cytotoxicity scores calculated using the*
839 *AddModuleScore function in Seurat using a list of the top 50 genes with expression correlated with that*
840 *of CD52 and IFNG respectively.* ***(c)*** *Distribution of cells from pre-treatment samples (C1) or d21 on-*
841 *treatment samples (C2) along the pseudotime map.* ***(d)*** *Changes in pseudotime upon ICB were assessed*
842 *using a linear mixed effect models with individual being fitted as a fixed intercept. Different branch*
843 *combinations of the pseudotime map were included to pinpoint the changes occurring. Filled points*
844 *and line ranges represent the estimated fold change in pseudotime upon treatment and standard error*
845 *respectively.* ***(e)*** *Changes in proportion of cells present in each pseudotime branch upon ICB across*
846 *each individual (n=7, two-sided Wilcoxon-ranked sign test).* ***(f)*** *Relative expression heatmap of genes*
847 *significantly associated with increasing pseudotime (adjusted p-value* $< 1x10^{-4}$*) from Branch A along*
848 *Branch B or Branch C (left and right respectively).* ***(g)*** *Volcano plot of differentially expressed genes*
849 *between effector cells (left) and EM cells (right) in Branch C vs Branch B of the trajectory map*
850 *(adjusted p-value* < 0.05*).* ***(h)*** *GOBP pathway analysis of significantly enriched pathways in the*
851 *differentially expressed genes between Branch C and B from (e) (adjusted p-value*<0.05*).* ***(i)*** *Violin*
852 *plots for expression of indicated genes across each* $CD8^+$ *T cell subset.*

853

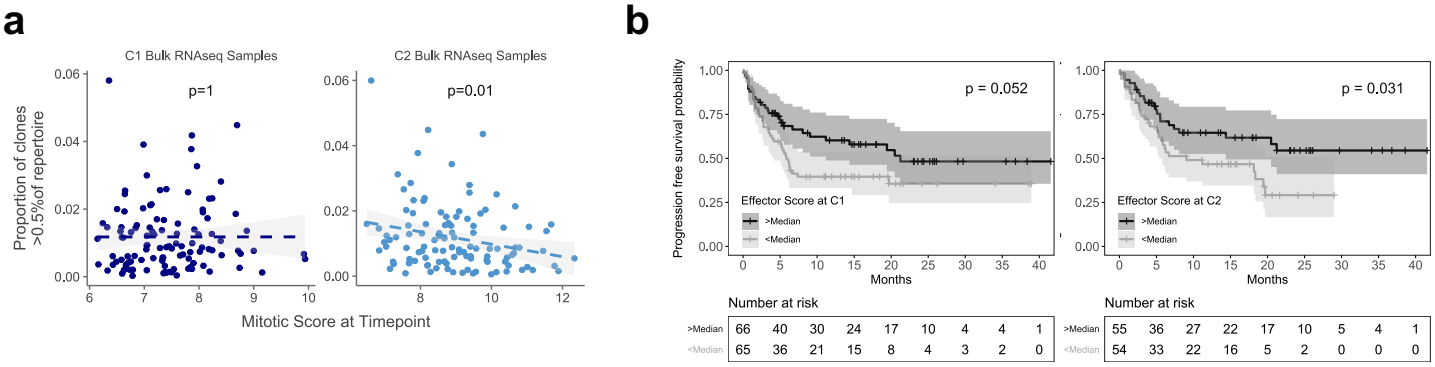

***Figure S5**: **Subset score associations with clonal and clinical characteristics. (a)** Pearson's correlation between calculated mitotic score in bulk RNAseq samples and the proportion of clones that occupy >0.5% of the TCR repertoire in those samples at C1 (left, n=111) and C2 (right, n=111). **(b)** Kaplan Meier curves of progression-free survival according to effector score at C1 (left, n=131) or C2 (right, n=109).*

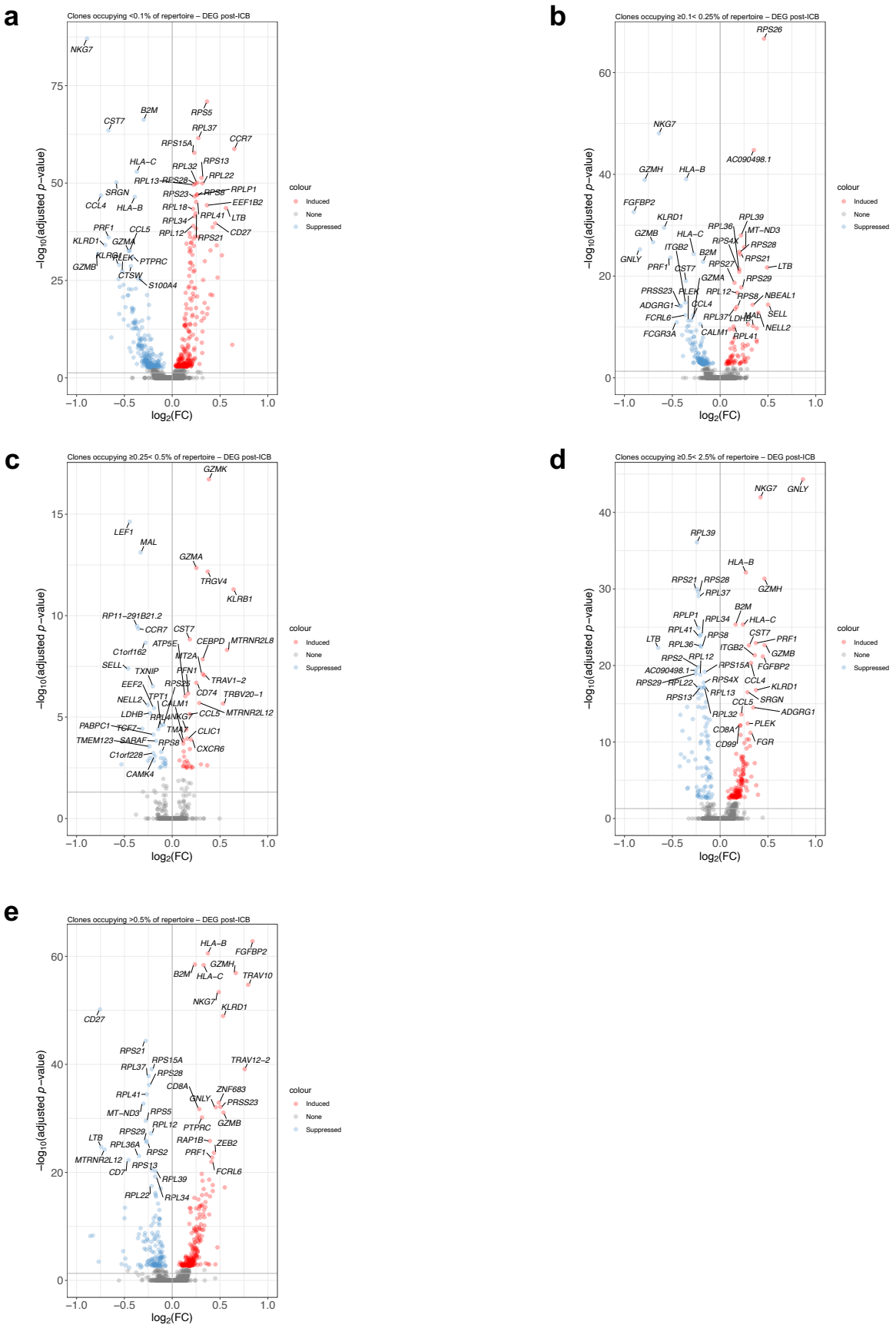

862 ***Figure S6: Differentially expressed genes across clonal categories. (a-e)*** *Volcano plots showing*

863 *DEGs for each clonal size category post ICB.*

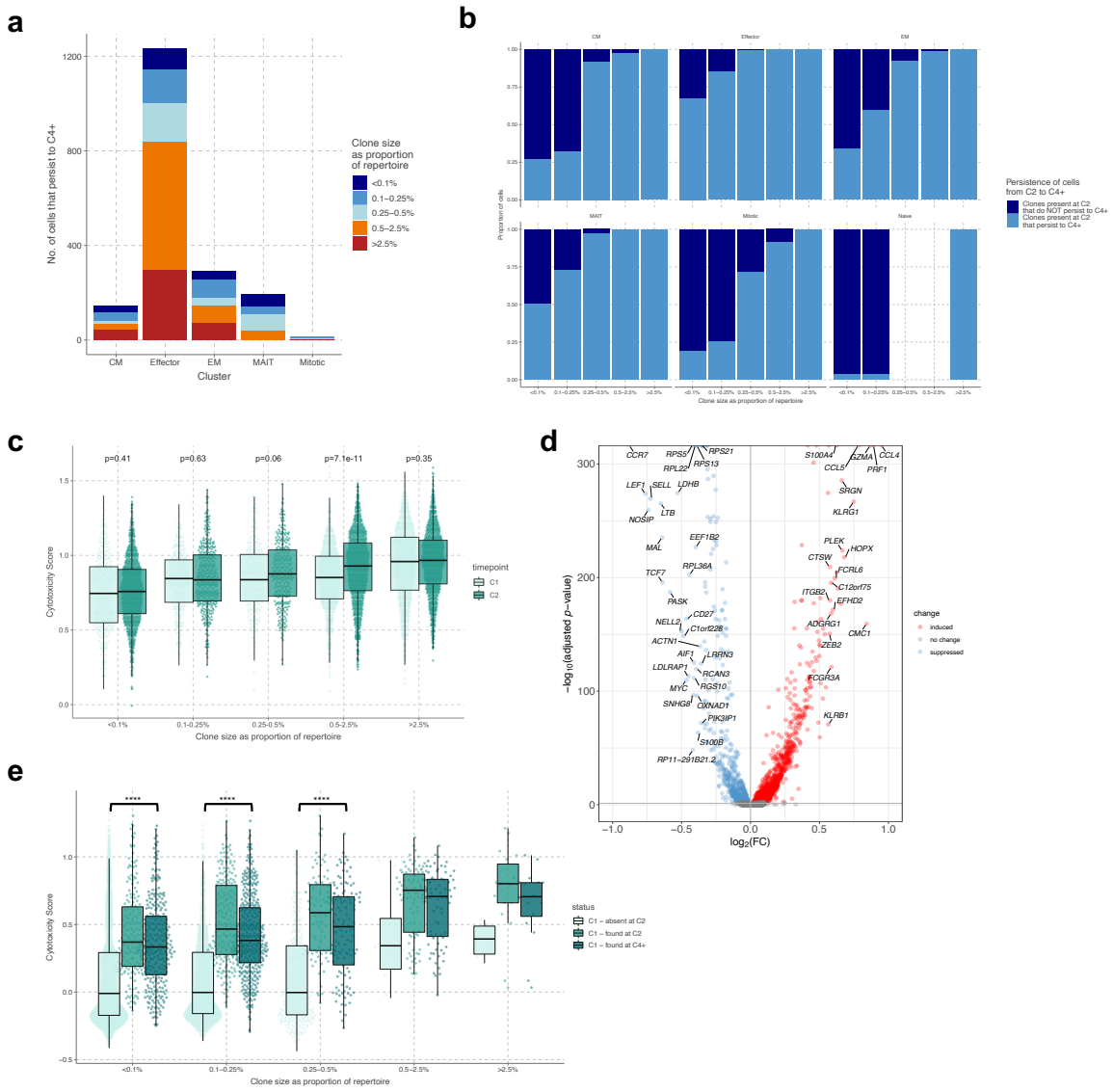

Figure S7: Clones present in peripheral blood at day 63+ are more cytotoxic and activated at baseline and day 21. ***(a)*** *Phenotypic cluster at baseline of clones that can be detected in peripheral blood at day 63+ (C4+), coloured by clonal size category.* ***(b)*** *Proportion of clones that persist to C4+ compared to those that do not persist, faceted by phenotypic subset and categorised by clonal size as proportion of repertoire.* ***(c)*** *Comparison of cytotoxicity scores for the ECs between C1 and C2, with analysis performed within clone size category (Two-sided Wilcoxon signed-rank test).* ***(d)*** *Volcano plot of differentially expressed genes between all cells at C2 that persist to C4+ versus those cells that do not persist.* ***(e)*** *Cytotoxicity score of cells at baseline, categorized as to whether they are only sampled at C1 versus if they are resampled at C2 or if they are found at C4+. ****adjusted p<0.0001. There is no*

874 *significant difference in cytotoxicity score between those persisting to C2 and those persisting to C4+,*

875 *except for cytotoxicity score in small clones (0.1-0.25% of repertoire, $p<0.05$).*

Donor	Age	Sex	Treatment	Cycle	Cells
1	82	M	sICB	C1	1731
				C2	2273
2	72	F	sICB	C1	439
				C2	1262
3	57	M	cICB	C1	1993
				C2	2004
4	45	F	cICB	C1	1028
				C2	643
5	43	F	sICB	C1	1391
				C2	1349
6	56	M	cICB	C1	28
				C2	2405
7	68	M	cICB	C1	1160
				C2	1224
8	69	M	sICB	C1	1925
				C2	1590

876

877 **Table S1: Donor characteristics and cell count per sample.**

878

Naïve	CM	EM	Effector	Mitotic
CCR7	LTB	GZMK	FGFBP2	TYMS
LEF1	GPR183	DUSP2	GZMH	RRM2
TCF7	CRIP2	CMC1	GZMB	MKI67
NOSIP	ARHGAP15	CD74	NKG7	CENPF
SELL	FXYD5	CCL5	KLRD1	UBE2C
AIF1	RCAN3	GZMA	ADGRG1	CENPM
ACTN1	NELL2	XCL2	PRF1	CDKN3
EEF1B2	FXYD2	RGS1	PRSS23	TK1
RPS5		TIGIT	SPON2	CLSPN
RPS13		FCRL3	ZEB2	GINS2
NPM1		COTL1	CX3CR1	
RPL32			ZNF683	
LRRN3			EFHD2	
RPS3A			FCRL6	
RPL22				

Table S2: Genes for bulk scores. List of genes used to generate scores (geometric mean) in $CD8^+$ T cell bulk RNAseq samples for each subset indicated.

885 **Data file S1 – included as separate file**

886 CSV file containing differentially expressed genes between large CD8+ T cell clones that persist

887 following ICB and those that do not persist

888 **Data file S2 – included as separate file**

889 CSV file containing lists of genes use to generate activation, exhaustion and cytotoxicity scores

890